Interplay Between Friction and Cohesion
A Spectrum of Retrogressive Slope Failure

Wang, Bin; Wang, Di; Hicks, Michael A.; Feng, Xia Ting

DOI
10.1029/2022JB026008

Publication date
2023

Document Version
Final published version

Published in
Journal of Geophysical Research: Solid Earth

Citation (APA)
Wang, B., Wang, D., Hicks, M. A., & Feng, X. T. (2023). Interplay Between Friction and Cohesion: A Spectrum of Retrogressive Slope Failure. *Journal of Geophysical Research: Solid Earth*, *128*(2), Article e2022JB026008. https://doi.org/10.1029/2022JB026008

JGR Solid Earth

RESEARCH ARTICLE
10.1029/2022JB026008

Interplay Between Friction and Cohesion: A Spectrum of Retrogressive Slope Failure

Bin Wang[1,2], Di Wang[1], Michael A. Hicks[3], and Xia-Ting Feng[4]

[1]Institute of Rock and Soil Mechanics, Chinese Academy of Sciences, State Key Laboratory of Geomechanics and Geotechnical Engineering, Wuhan, China, [2]University of Chinese Academy of Sciences, Beijing, China, [3]Section of Geo-Engineering, Faculty of Civil Engineering and Geosciences, Delft University of Technology, Delft, The Netherlands, [4]Key Laboratory of Ministry of Education on Safe Mining of Deep Metal Mines, Northeastern University, Shenyang, China

Key Points:

- Hierarchical multiscale modeling is carried out to explore the mechanism of various retrogressive failure modes in granular slopes
- The interplay between friction and cohesion near the slope surface determines the development of earth flow or flowslide failure pattern
- The friction effect controls the bottom of slopes and contributes to the translational shear band and the spread failure of slopes

Correspondence to:
D. Wang,
dwang@mail.whrsm.ac.cn

Citation:
Wang, B., Wang, D., Hicks, M. A., & Feng, X.-T. (2023). Interplay between friction and cohesion: A spectrum of retrogressive slope failure. *Journal of Geophysical Research: Solid Earth*, *128*, e2022JB026008. https://doi.org/10.1029/2022JB026008

Received 15 NOV 2022
Accepted 22 JAN 2023

Author Contributions:
Conceptualization: Bin Wang, Di Wang, Xia-Ting Feng
Formal analysis: Bin Wang, Di Wang, Michael A. Hicks
Funding acquisition: Bin Wang, Di Wang, Xia-Ting Feng
Investigation: Bin Wang, Di Wang
Methodology: Bin Wang, Di Wang
Software: Bin Wang, Di Wang
Supervision: Bin Wang, Di Wang, Michael A. Hicks, Xia-Ting Feng
Validation: Bin Wang, Di Wang
Visualization: Bin Wang, Di Wang
Writing – original draft: Bin Wang, Di Wang
Writing – review & editing: Bin Wang, Di Wang, Michael A. Hicks, Xia-Ting Feng

Abstract Retrogressive failures occur in slopes consisting of sensitive materials such as snow or quick clay. They can be triggered by a small disturbance at the slope toe, but can cause propagated failure spreading miles away. Understanding the physical mechanism and predicting the retrogressive failure process are particularly important. Previous studies have discussed the failure criteria, the soil properties or the method of numerical modeling of retrogressive slope failure. However, little attention has been paid to the microscopic failure mechanism, especially relating to various possible failure patterns. In this study, multiscale modeling is incorporated to study the physical mechanism of different retrogressive failure patterns, including earth flow, flowslide and spread failure, within a unified framework. Utilizing multiscale analysis, we found that earth flow failure is related to the shear failure of granular materials. In contrast, the development of macroscopic shear bands is accompanied by tensile failure. As shear and tension failures are typical failure mechanisms of frictional and cohesive materials, it is deduced that friction and cohesion effects play key roles in different retrogressive failure patterns. Therefore, the distributions of attractive and repulsive contact forces are explored and a novel parameter η is proposed to quantify the interplay between friction and cohesion. Further analysis proves that η can capture the effect of friction and cohesion and distinguish different retrogressive failure patterns. Finally, a spectrum of retrogressive failures for a granular slope is established, in which the failure mechanism is explained by the changeable dominant effect, that is, frictional or cohesive in soil.

Plain Language Summary Slope failure is a common geo-hazard that occurs in nature and engineering. For example, a sensitive clay consisted soil slope can easily propagate for miles, leading to catastrophic damage to human lives and properties. Previous researchers mainly study the slope failure processes/mechanisms on the scale of soil blocks, lacking observations at the soil particle scales. In this research, a hierarchical multiscale modeling is proposed, which enables the simulation of both the retrogressive slope failure process and interactions between soil particles. The mechanisms of various retrogressive failure patterns are thereby explored, including earth flow, flowslide, and spread failure. The earth flow tends to fail near the surface by shearing, where the shear strength is mainly determined by the friction between particles. The flowslide fails in a retrogressive pattern, shown as bulks of soils moving after bulks. The soil in shear bands fails under stretching mainly, where the strength is determined by the cohesion between particles. The spread failure is more complex, combining the influences of friction and cohesion. The friction effect controls the bottom of slopes, contributing to the translational shear band and spread failure of slopes. A spectrum to classify different failure patterns is established at the end.

1. Introduction

Landslides are natural hazards that may show diverse and complicated triggering and failure processes, such as advancing, enlarging, progression, and retrogression, due to varying soil properties, slope geometry or environments, etc (Varnes, 1958). Among the different failure patterns, retrogressive failure is characterized by a series of rearward-advancing disruptions of a slope after triggering by a small initial failure at the toe. The sequential failure can spread miles away from the starting point, as reported by Locat et al. (2011). In literature, retrogressive slope failures are mostly observed and discussed in relation to the failure of sensitive clay (Carson, 1979; Locat et al., 2011; Mitchell & Markell, 1974; Quinn et al., 2012) or soils which are cohesive with plastic behavior (Chandel et al., 2021; Cuomo et al., 2019; Qi et al., 2018; Richer et al., 2020; Xu et al., 2011). It is also a meaningful topic in submarine landslides and dredging processes (Eke et al., 2011; Puzrin et al., 2017; Van Den Berg

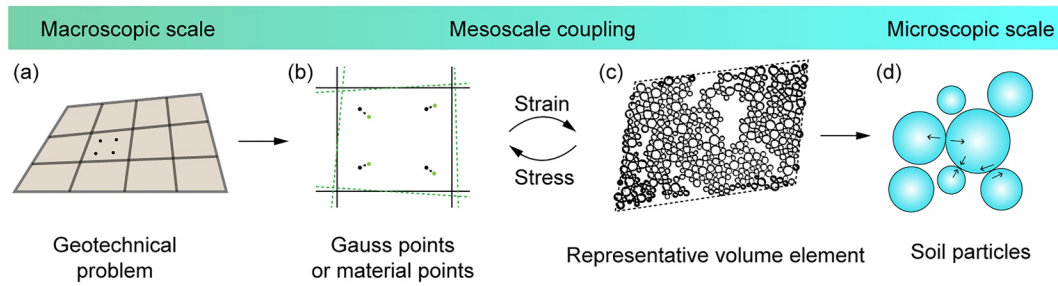

Figure 1. Framework for hierarchical multi-scale modeling in the simulation of geotechnical problems.

et al., 2002; W. Zhang & Puzrin, 2021), and related to substantial tsunamis when occurring at the continental margins (Glimsdal et al., 2016; Løvholt et al., 2015).

To prevent damage from these retrogressive failure processes, understanding the mechanism and predicting the process of retrogressive failure is of significant importance. Topics such as triggering mechanism (Lo, 1972; Locat et al., 2011), failure criteria (Germanovich et al., 2016; Puzrin et al., 2017; W. Zhang et al., 2016), development process (Quinn et al., 2012) and run-out distance (Puzrin, 2016) have been widely studied. It is found that the retrogressive failure may show several typical failure types, such as flow, translational progressive landslides and spread. The topography and geological history are major factors in triggering the failure, and the strain-softening behavior of soil may also influence the development process (Locat et al., 2011). Many empirical and analytical criteria have been proposed to determine the stability of slopes, but their application is limited due to the simplified assumptions and complex destabilizing factors of natural slopes. If the soil is temperature sensitive, the friction softening effect may significantly reduce the shear strength of the soil, thereby causing a relatively low-impact slope failure to lead into a catastrophic landslide (Goren & Aharonov, 2007; Paesold et al., 2016; Vardoulakis, 2002). To give a more accurate assessment of retrogressive slope failure, numerical methods have been utilized, for example, by using the large deformation finite element method (Dey et al., 2015; D. Wang et al., 2013), the material point method (MPM; B. Wang et al., 2016), and the particle finite element method (X. Zhang et al., 2018), among others. It is also necessary to incorporate a rate-dependent constitutive model to capture the strain-softening behavior of soil (X. Zhang et al., 2018). With the appropriate numerical model, the development of retrogressive failure may be well reproduced, contributing to the analysis of the slope failure propagation.

However, most previous studies have focused on the description and simulation of the retrogressive failure process with theoretical or numerical modeling. Little attention has been given to the underlying microscopic failure mechanism. Therefore, in this paper, a multiscale modeling method is incorporated based on a hierarchical coupling between the MPM and the discrete element method (DEM), with the aim of building a unified description of different retrogressive failure patterns and an understanding of the microscopic physical mechanism. More specifically, MPM can well describe the large deformation process of the retrogressive failure, while, on the other hand, DEM can capture the complex mechanical behavior of granular materials such as history-dependence or rheology, etc., without relying on phenomenological constitutive models. Via the multiscale modeling of granular slopes with different inclination angles, three typical retrogressive failure patterns are reproduced. By analyzing the microscopic properties of representative volume elements in each retrogressive failure pattern, two major failure mechanisms are recognized as shear and tensile failure. Through investigation of the repulsive and attractive contact force distributions, it is found that the interplay between friction and cohesion plays a significant role in different failure patterns. A novel parameter η is proposed to quantify the effect of friction and cohesion of granular materials. Further analysis proves that η can effectively act as an indicator to distinguish different retrogressive failure patterns. Finally, a spectrum of retrogressive slope failures is proposed and discussed based on the simulation results.

2. Methods

Hierarchical multiscale modeling (HMM) involves macro, meso, and microscopic simulation based on continuum and discrete numerical theories (N. Guo & Zhao, 2014). The simulation framework of HMM is displayed in Figure 1, which includes three major components, that is, macroscopic scale, microscopic scale, and mesoscale coupling.

Macroscopic Scale

The macroscopic scale component considers the description and simulation of the boundary value problem, that is, the slope failure process in this study (as indicated in Figure 1a). It relates to the discretization of the slope geometry, the application of boundary conditions and the capturing of deformations and movements.

Microscopic Scale

The microscopic simulation aims to reproduce an appropriate stress-strain response based on the mechanical response of soil particles. It facilitates a more accurate reproduction of different failure patterns and provides more detailed information for understanding the underlying failure mechanism.

Mesoscale Coupling

The mesoscale coupling is realized by a representative volume element (RVE). The RVEs are composed of particle assemblies in a periodic element, with a size that is much smaller than the macroscopic geometry to reflect the spatial variation of loading state and material properties, and also much larger than the particle size to include a sufficient number of micro-features and to represent a typical mechanical response. During the simulation, the RVEs inherit the deformation from the macroscopic scale, and apply it to the particle assemblies inside the RVEs. Conversely, via the rearrangement of the particles inside the RVEs, a new stress state is thereby generated which can then be transferred to macroscopic elements as a stress tensor. Therefore, with the RVEs, the macro and microscopic scale simulations are coupled (see Figures 1b and 1c), forming a multiscale simulation framework.

Generally, HMMs have now been widely employed in the study of geotechnical problems (Liang & Zhao, 2019a, 2019b; H. Wu et al., 2017, 2020, 2018). Different coupling methods have been proposed, such as FEM/DEM, MPM/DEM, and SPFEM/DEM (N. Guo, Yang, et al., 2021; N. Guo & Zhao, 2014; X. Guo, Peng, et al., 2021; Liu et al., 2017), in fulfilling the various requirements of different geotechnical analyses. In this paper, to capture the whole slope failure process, a coupled MPM/DEM method for slope failure analysis has been utilized, for which the numerical implementation has been validated quantitatively (D. Wang et al., 2022). A brief introduction to the formulation of the coupling method is first presented for the sake of completeness. The MPM solver is developed by Taichi language (Hu et al., 2019), and the opensource software LIGGGHTS (Kloss et al., 2012) is used for DEM modeling.

2.1. MPM Solver

In MPM, the governing equations concern mass and momentum conservation, and are expressed as follows:

$$\frac{d\rho}{dt} + \rho\nabla\boldsymbol{v} = 0 \tag{1}$$

$$\rho\boldsymbol{a} = \nabla\boldsymbol{\sigma} + \rho\boldsymbol{b} \tag{2}$$

where ρ is the material density, $\boldsymbol{v}$ and $\boldsymbol{a}$ are the material velocity and acceleration, respectively, $\boldsymbol{\sigma}$ is the Cauchy stress tensor and $\boldsymbol{b}$ is the specific body force, for example, gravitational force. All of these parameters are functions of the time t and material point coordinates $\boldsymbol{x}$, that is, $\rho = \rho(\boldsymbol{x}, t)$. The continuum problem is discretized into material points with prescribed mass, velocity, acceleration, etc., where the mass conservation (Equation 1) is satisfied theoretically. Equation 2 is solved by discretization of its weak form, which can be written as follows:

$$\int_\Omega \rho\omega\boldsymbol{a}\, d\Omega + \int_\Omega \boldsymbol{\sigma}\nabla\omega\, d\Omega = \int_\Omega \rho\omega\boldsymbol{b}\, d\Omega + \int_\Gamma \rho\boldsymbol{\tau}\omega\, d\Gamma \tag{3}$$

where Ω and Γ represent the computational domain and its boundary, respectively, ω is the test function and $\boldsymbol{\tau}$ is the specific traction acting on the surface Γ.

After the initial discretization, the particle mass m_p assigned to each material point can be expressed as follows:

$$m_p = \int \rho(\boldsymbol{x}, t)\delta(\boldsymbol{x} - \boldsymbol{x}_p)\, dV_p \tag{4}$$

where V_p is the volume and $\boldsymbol{x}_p$ are the spatial coordinates of material point p. The sum of the mass of the particles equals the actual mass of the continuum:

$$\sum_p m_p = \sum_p \int \rho(\boldsymbol{x}, t)\delta(\boldsymbol{x} - \boldsymbol{x}_p)\, dV_p = \int \rho(\boldsymbol{x}, t)\, d\Omega \tag{5}$$

Similar to mass, the material point properties such as velocity, momentum, and stress can also be expressed in a summation manner. Equation 3 can thereby be rewritten as follows:

$$\sum_p m_p \omega(\boldsymbol{x})\boldsymbol{a}(\boldsymbol{x}) + \sum_p m_p \boldsymbol{\sigma}(\boldsymbol{x}) : \nabla\omega(\boldsymbol{x}) = \sum_p m_p \omega(\boldsymbol{x})\boldsymbol{b}(\boldsymbol{x}) + \sum_p m_p \omega(\boldsymbol{x})\boldsymbol{\tau}(\boldsymbol{x})h^{-1} \tag{6}$$

where h is the presumed boundary layer thickness for the calculation of external force due to traction.

In MPM the gradient terms are calculated on a background grid. For the information transfer between material points and the background grid, standard finite element shape function $N_i(\boldsymbol{x}_p)$ are normally utilized. The coordination or kinematic variables $f(\boldsymbol{x})$ of any material point can be represented by:

$$f(\boldsymbol{x}_p) = \sum_i N_i(\boldsymbol{x}_p) f(\boldsymbol{x}_i) \tag{7}$$

where $\boldsymbol{x}_i$ refers to the coordinates of grid nodes surrounding the material point p. Due to their discontinuous nature at inter-element boundaries, traditional linear shape function generates cross-cell instabilities. For overcoming this problem, a quadratic B-spline shape function is incorporated in this paper.

Substituting Equation 7 into Equation 6, the discretized weak form of the equation can be given as follows:

$$\boldsymbol{M}\boldsymbol{a} = \boldsymbol{F}_{\text{int}} - \boldsymbol{F}_{\text{ext}} \tag{8}$$

where $\boldsymbol{M}$ is the nodal lumped mass matrix, and $\boldsymbol{F}_{\text{int}}$ and $\boldsymbol{F}_{\text{ext}}$ are the internal and external nodal force vectors, respectively. The nodal acceleration at each grid node is thereby solved and the nodal velocity is updated sequentially. Correspondingly, the position and velocity of material points can be updated. To reduce numerical diffusion, the particle position is updated according to the nodal velocity:

$$\boldsymbol{x}_p^{t+1} = \boldsymbol{x}_p^t + \sum_i N_i\left(\boldsymbol{x}_p^t\right)\boldsymbol{v}_i^t \Delta t \tag{9}$$

For better energy conservation, an affine-particle-in-cell (APIC) format is utilized in this paper for updating the material point velocity, which considers both the linear and angular momentum. In APIC, the PIC format is used for the velocity update from grid cells to material points, that is, $\boldsymbol{v}_p^{t+1} = \sum_i N_i\left(\boldsymbol{x}_p^t\right)\boldsymbol{v}_i^t$. In addition, a local affine matrix $\boldsymbol{C}_p = \boldsymbol{B}_p\boldsymbol{D}_p^{-1}$ is updated by the inertia matrix $\boldsymbol{D}_p$ and angular momentum information $\boldsymbol{B}_p$:

$$\boldsymbol{B}_p^t = \sum_i N_i\left(\boldsymbol{x}_p^t\right)\boldsymbol{v}_i^t\left(\boldsymbol{x}_i^t - \boldsymbol{x}_p^t\right)^{\mathrm{T}} \tag{10}$$

$$\boldsymbol{D}_p^t = \sum_i N_i\left(\boldsymbol{x}_p^t\right)\left(\boldsymbol{x}_i^t - \boldsymbol{x}_p^t\right)\left(\boldsymbol{x}_i^t - \boldsymbol{x}_p^t\right)^{\mathrm{T}} = \frac{L^2\boldsymbol{I}}{4} \tag{11}$$

where L is the grid length and $\boldsymbol{I}$ is the unit matrix. When the material point momentum is transferred to the background cells, the following scheme is employed:

$$m_i\boldsymbol{v}_i^t = \sum_p m_p N_i\left(\boldsymbol{x}_p^t\right)\left(\boldsymbol{v}_p^t + \boldsymbol{C}_p^t\left(\boldsymbol{x}_i^t - \boldsymbol{x}_p^t\right)\right) \tag{12}$$

2.2. DEM Solver

The microscopic mechanical behavior of granular materials is simulated by DEM, where the interactions between particles are represented by the contact forces. In this study, three types of contact forces, that is, Hertzian normal

contact force F_h, tangential frictional force F_t and adhesive force F_a, are considered by employing the Hertzian contact model, Johnson-Kendall-Roberts cohesive model and Coulomb friction law, respectively:

$$F_h = k_n \delta\varepsilon_n \tag{13}$$

$$F_a = k_a a \tag{14}$$

$$F_t = \begin{cases} \min\{k_t \delta\varepsilon_t, \mu(F_h - F_a)\}, & F_h > F_a \\ 0, & F_h < F_a \end{cases} \tag{15}$$

where k_n, k_t are the normal and tangential stiffnesses, respectively, k_a is the cohesion energy density, $\delta\varepsilon_n$ and $\delta\varepsilon_t$ refer to normal and tangential overlaps, $a = 4\pi\delta\varepsilon_n R^*$ is the contact area of two contacting particles, where $R^* = R_1 R_2/(R_1 + R_2)$ is the harmonic mean of two contacting particle radii, and μ is the inter-particle friction coefficient. The normal and tangential stiffnesses are calculated as follows:

$$k_n = \frac{4}{3} E^* \sqrt{R^* \delta\varepsilon_n} \tag{16}$$

$$k_t = 8G^* \sqrt{R^* \delta\varepsilon_n} \tag{17}$$

where E^* and G^* are the equivalent Young's modulus and shear modulus, respectively, computed using the Young's modulus and the Poisson's ratio of the particles:

$$\frac{1}{E^*} = \frac{\left(1 - \nu_1^2\right)}{E_1} + \frac{\left(1 - \nu_2^2\right)}{E_2} \tag{18}$$

$$\frac{1}{G^*} = \frac{2(2 - \nu_1)(1 + \nu_1)}{E_1} + \frac{2(2 - \nu_2)(1 + \nu_2)}{E_2} \tag{19}$$

2.3. Mesoscale Coupling Method

In HMM, each material point is built with an RVE to capture the stress-strain response and record the stress-strain history. The coupling is realized by the communication of information between the material points and RVEs in each step. During the simulation, the load is first applied in MPM and this produces deformations on the material points. The deformation gradient $\boldsymbol{F}_p$ is calculated from the macroscopic variables in MPM as follows:

$$\boldsymbol{F}_p^{t+1} = (1 + \nabla \boldsymbol{v}_p \Delta t)\boldsymbol{F}_p^t \tag{20}$$

Then, the deformation gradient is applied to the RVEs as a boundary condition in DEM and the shape of the RVE will deform from $\boldsymbol{F}_p^t$ to $\boldsymbol{F}_p^{t+1}$ in the prescribed time step. After the deformation, the positions and contacts of the particles change, showing different mechanical responses, that is, macroscopic stress state. As the RVEs are assembled as a group of particles, an equivalent estimation of the stress tensor of the particle assembly in the RVEs is necessary for the coupling. In this study, the stress tensor is obtained from Love's formula (Nicot et al., 2013), defined as follows:

$$\boldsymbol{\sigma} = \frac{1}{V} \sum_{N_c} \boldsymbol{d} \otimes \boldsymbol{F} \tag{21}$$

where V is the volume of the RVE, N_c indicates the number of contacts within the packing, $\boldsymbol{d}$ is the branch vector and $\boldsymbol{F}$ is the total contact force of two contacting particles. Finally, the stress state of the element is returned to the MPM, and the macroscopic simulation continues until the next communication. For more detailed information on the MPM-DEM coupling method, the reader is referred to D. Wang et al. (2022).

As the material mechanical behavior of an element is represented by RVEs, the damage and failure of elements are also captured by the state of the granular assembly. In this study, the fragmentation and damage of particles

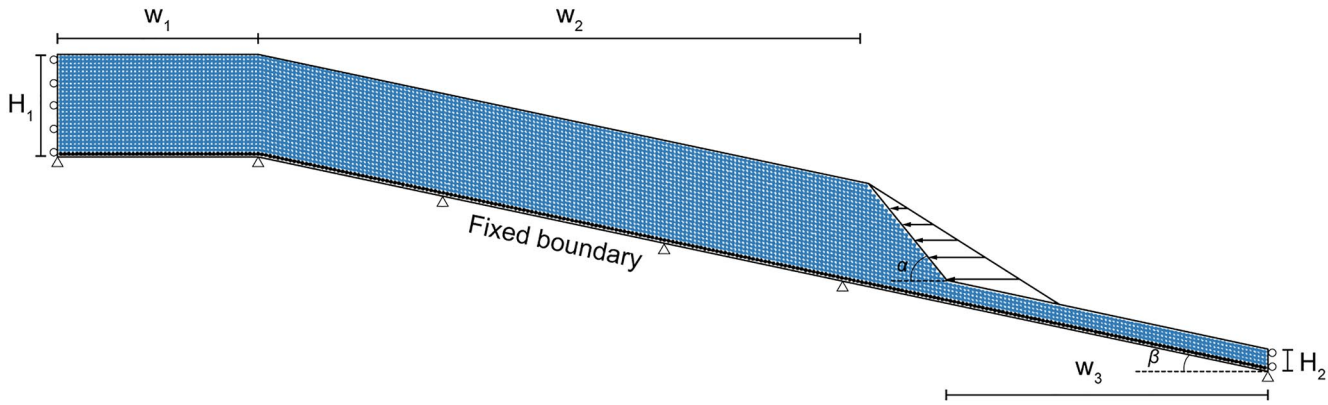

Figure 2. Sketch of the initial slope geometry.

are not considered for simplicity; rather, the macroscopic failure and damage are derived from the rearrangement of particles. To characterize the intensity of the rearrangement of RVEs and represent the developing macroscopic material plasticity, a mesoscale parameter, the granular temperature T (Zou et al., 2022), is introduced:

$$T = \frac{1}{D}\langle \delta \boldsymbol{v} \cdot \delta \boldsymbol{v} \rangle \tag{22}$$

where δv is the fluctuating velocity and D is the dimension of the simulation ($D = 2$ in this study). The fluctuating velocity is defined as the velocity difference between particle i and the corresponding neighboring particle, that is, $\delta \boldsymbol{v} = \boldsymbol{v}_i - \boldsymbol{v}_{\text{neigh}}$. The value of T ranges from 0 to infinitely large. For a high granular temperature, the rearrangement activities of particles are intensive, indicating plastic deformation. Conversely, low granular temperature means that particles deform with no rearrangement, so that the macroscopic deformation is elastic.

2.4. Model Setup

A long slope on a rigid inclined foundation is incorporated as the typical profile based on previous studies (Vardon et al., 2017; B. Wang et al., 2016, 2018), as shown in Figure 2. A total of 5,710 material points is generated, with each material point initially representing a space of $0.2 \times 0.2\,\text{m}^2$ (equal to grid cell size), to discretize the slope. The initial geometry of slope is 5 m depth (H_1) and 30 m long (W_2) inclined at an angle β. A horizontal section with a length of $W_1 = 10\,\text{m}$ is located at the top of the slope to avoid boundary effects. The depth of the slope near the toe decreases linearly to 1 m over an approximately horizontal distance of 4 m (depending on the angle α, where $\alpha = 45° + \beta$), and then forms a shallow soil layer with a length of $W_3 > 15\,\text{m}$ and depth of $H_2 = 1$ m. The left and right-hand edges of the simulation domain are designated roller boundaries to prevent horizontal movement while allowing vertical displacement. The bottom boundary is fully fixed to simulate a rough interface with the bedrock below. A gravitational acceleration ($g = 9.8\,\text{m/s}^2$) is applied to the whole domain and a confining stress is applied at the toe in the first 2 s, to generate the initial stress field. The confining stress is then removed to trigger failure of the slope.

Table 1
Discrete Element Method Modeling Parameters of Representative Volume Elements

Property	Value
Particle density ρ	2,900 kg/m^3
Particle diameter d	3–7 mm
Young's modulus E	600 MPa
Poisson's ratio ν	0.4
Particle restitution coefficient e	0.8
Particle friction coefficient μ	0.02
Cohesion energy density k_a	9,000 KJ/m^3

The soil properties are the primary factor that influences the development of the retrogressive failure. In HMM, the soil is represented by granular particles, where the deformation is due to the rearrangements of particles and the stress is dominated by contact forces. Therefore, it is important to build an RVE model that appropriately reflects the key characteristics of the soils.

To simulate the typical progressive failure process of the natural slope, a granular RVE resembling the soil properties of a sensitive clay, with a low friction but a relatively high cohesion, has been built. The friction and cohesion are controlled by inter-particle friction and adhesive forces in the microscopic view. In DEM modeling, the friction coefficient μ limits the maximum tangential contact forces F_t between particles, that is, $F_t \leq \mu F_r$ (where

F_r is the repulsive contact force). The adhesive force is determined by the cohesion energy density k_a. In our modeling, the RVE parameters are chosen as shown in Table 1, with a very small $\mu = 0.02$ and a relatively high $k_a = 9,000\,\mathrm{KJ/m^3}$.

It is known that clay consists of particles with a size of micro-meters or even smaller, which is difficult to simulate directly by tracking the motion of each particle. A possible method is to regard the DEM particles as clumps of clay particles with a larger size. The particle size should perform the macroscopic response appropriately and reflect the microscopic cracking behavior. As suggested by Sima et al. (2014), the radius can be several mm. Therefore, the particle diameter in the paper is set as 3–7 mm with a uniform distribution. 400 particles are included in each RVE with an initial size of $0.17 \times 0.17\,\mathrm{m^2}$, which is a bit smaller than the space initially represented by one material point.

A series of RVE biaxial tests are carried out with the prescribed RVE parameters. The RVEs are confined under a stress σ_p between 50 and 200 kPa and the loading rate γ (i.e., $\dot{\epsilon}_{yy}$) is 0.01 $\mathrm{s^{-1}}$ (as shown in Figure 3a). The corresponding stress-strain responses are plotted in Figure 3b. It can be found that the particle assembly shows a jagged response in Figure 3b due to the number of particles being relatively small and the particle size being relatively large compared to the domain size. According to the Mohr circles plotted in Figures 3c–3d (which are based on a simple, approximate interpretation of the response in Figure 3b), the peak and residual cohesions of the granular materials are $c_p = 15\,\mathrm{kPa}$ and $c_r = 6\,\mathrm{kPa}$, respectively. Hence, the granular assembly shows a relatively low residual cohesion, with a strain softening behavior that is crucial to retrogressive failure. The peak and residual friction angles are $\phi_p = 10°$ and $\phi_r = 9°$, indicating only a slight decrease. Note that, even though the inter-particle friction coefficient is very small, the friction angle does not reach an extremely low value. The friction may result from the adhesive contact forces between particles, which leads to larger normal and tangential contact forces compared to a cohesionless system.

3. Retrogressive Failure of an Inclined Slope

In this section, the retrogressive failure of granular slopes is simulated with the prescribed HMM method and RVE properties. The slope failure is triggered by removing the confining stress at the slope toe and the inclination angle β is varied to generate different stress states within the granular slope, resulting in different failure patterns.

3.1. Type 1: Earth Flow

A slope with a 6° inclination angle is presented in Figure 4. Slope failure is triggered with the development of a shear band at the toe. Then, the retrogressive failure develops in the manner of an uphill-propagating avalanche, where no further shear band or localization can be observed. The simulated failure process lasts for around 40 s and continues until it reaches the slope crest. During the failure process, the retrogressive wave speed is initially 1.18 m/s and it then decays with time as indicated in Figure 4.

This failure mode is very similar to earth flow in landslides. The soil starts to fail at the surface, then destabilizes and causes retrogressive failure without the localization of strains into shear bands. Earth flows are very common in dry granular materials (e.g., stockpiles of sand or the lee slopes of sand dunes) and can also occur in soils with a certain moisture content (e.g., banks of sand or silt). Daerr and Douady (1999) conducted failure experiments on a cohesionless granular material on an inclined plate and reproduced the retrogressive failure process of an earth flow. Friction hysteresis, that is, the difference between the maximum (static) and minimum (dynamic) friction coefficients, was found to be one of the most important factors determining the failure process. The development of failure can be very slow when the difference between the maximum and minimum friction coefficients is small and this is consistent with the simulation in this study. Due to the small difference between the peak friction angle and the residual friction angle of the material, the development of the failure in the slope is significantly slower than for the other failure modes investigated.

3.2. Type 2: Flowslide

We next increase the inclination angle of the slope to 10°, approaching the soil friction angle. It can be seen that, once again, the retrogressive failure starts with shear band initiation in the vicinity of the slope toe; in this case,

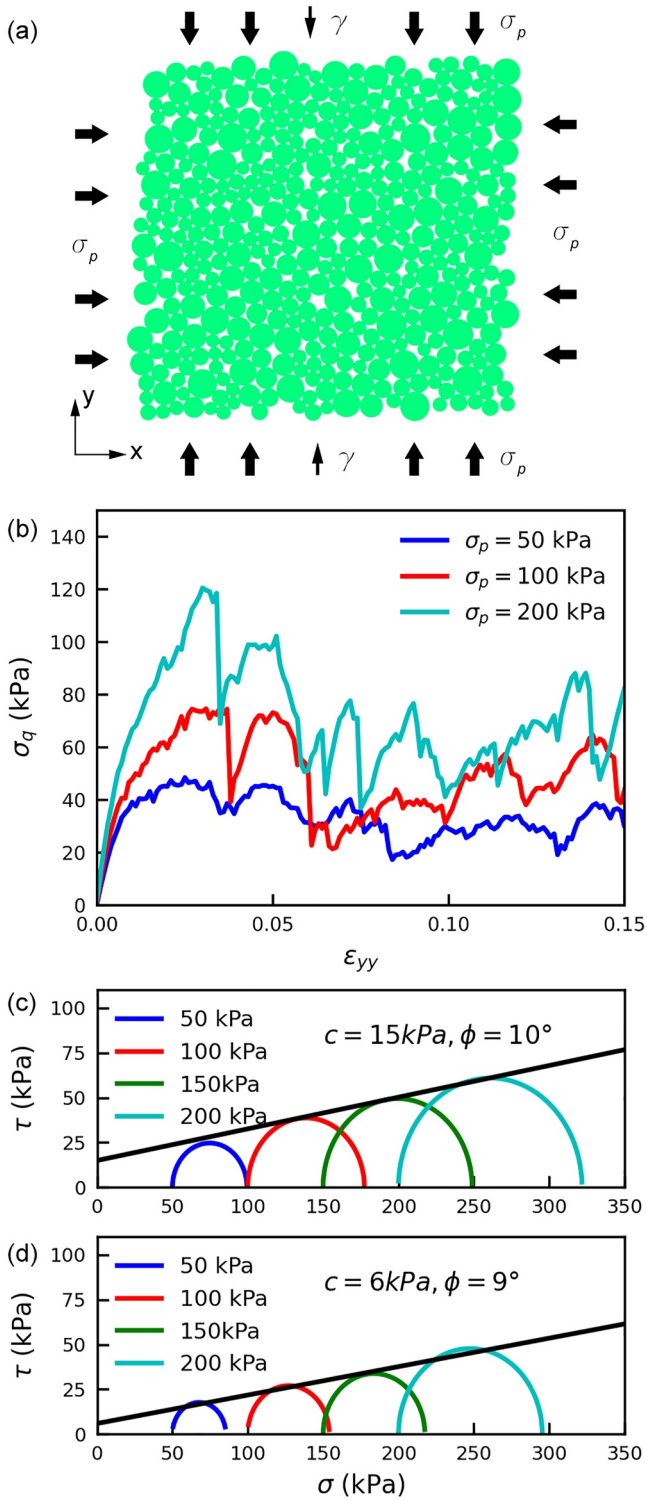

Figure 3. Representative volume element (RVE) biaxial test results. (a) Setup of RVE biaxial test. (b) Stress-strain curves under different confining stresses, where σ_q is the deviatoric stress. (c) Mohr circles at peak stress state. (d) Mohr circles at residual stress state.

with the formation of two shear bands (S1 and S2 as shown in Figure 5a). Then, retrogressive failure develops backward with successive shear bands. Specifically, the failure process involves the formation of another two shear bands (S3 and S4) near to each other, at $t = 2$ s and $t = 6$ s, as indicated by the dashed lines in Figures 5b–5c. At $t = 10$ s, toward the end of the simulation, a shear band S5 starts to form near the top of the slope (as shown in Figure 5d). Unlike the earth flow failure mode, the failure process in Figure 5 indicates multiple shear bands propagating from the base of the soil layer to the slope crest.

This failure mode is the typical retrogressive failure observed in sensitive clay or loess (Locat et al., 2011; Qi et al., 2018; Quinn et al., 2012), known as a flowslide. Similar to the earth flow, this type 2 failure pattern also originates from the removal of support due to the first slide. However, instead of an overall transition to an earth flow, the failure process involves multiple slides until the final stable scarp is reached. This type of failure is mainly dominated by the stress distribution and the stress-strain response of the soil. As indicated by Tavenas (1984), three major factors lead to a flowslide: (a) an initial slide occurs; (b) the potential energy of the failed soil is high enough to remold the clay; (c) the remoulded clay shows significantly lower shear strength. In this simulation, the retrogressive slope failure is triggered by a toe cut which causes an initial slide. Then, a high granular temperature is observed in the shear band, indicating the intensive plastic deformation of materials. Finally, the granular materials show a ratio of $c_p/c_r = 2.5$ between the peak and residual cohesions, which means a significant reduction in shear strength when sheared to a certain strain. Moreover, the inclination angle β is approximately equal to the friction angle, which means that the frictional property of the soil is balanced under gravity. This suggests that the cohesion effect may be the major factor controlling the development of the shear band propagation.

3.3. Type 3: Spread

If we further incline the slope to $\beta = 15°$, which is larger than the friction angle of the soil, a long translational shear band (S6) is first seen propagating along the basal boundary after the initial failure is triggered (Figure 6a). After 3 s, several secondary shear bands are seen to have initiated inside the moving bulk, dividing the landslide into several parts (Figure 6b). If we look in detail into the propagation of the shear bands at 2 s, as shown in Figure 6e, it is found that there are three shear bands S1–S3 developing in approximately parallel directions, whereas shear band S5 is more gently inclined, with an inclination in between S1 and that of the top shear band S6. Between S3 and S5, a weakly developed shear band S4 appears but it is not fully developed until 5 s. After 4 s of sliding, reverse shear bands have been formed as shown in Figure 6c, resulting a pattern of horsts and grabens as seen in Figure 6d. These reverse shear bands are nearly perpendicular to shear bands S1-S6 and propagate from the two end shear bands (S1 and S6) inward as illustrated by the arrows in Figure 6f. It can be seen that reverse shear bands RS1 and RS5 are developing at $t = 3$ s, while RS3 and RS4 show only slight increases of granular temperature, which indicates the initiation of the shear bands. At the position of RS2, no reverse shear band is observed until $t = 5$ s. Therefore, the development of these shear bands does seem to initiate from the two ends of the soil layer and then develop inwards during the progressive failure (as indicated by the arrows in Figure 6f).

This failure pattern is widely observed in nature (Locat et al., 2011) and is usually known as a spread failure or downward progressive failure. The

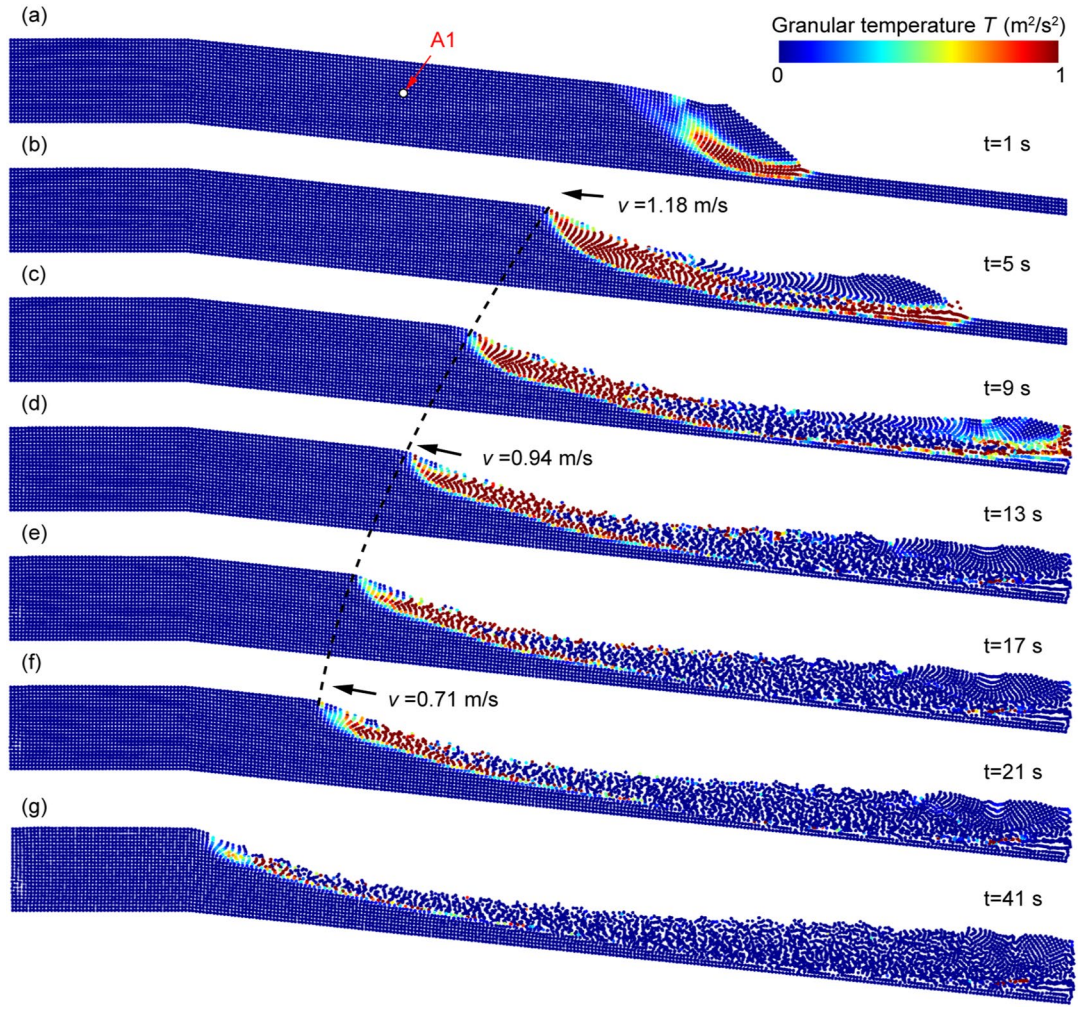

Figure 4. Earth flow for a slightly inclined slope. Label A1 indicates the location of an representative volume element.

typical characteristics of a spread failure are the underlying translational failure surface and the development of horsts and grabens. In nature, the underlying (i.e., translational) failure surface is probably caused by water flow or erosion, whereas in this simulation the large inclination angle leads to the initiation of failure at the contact surface between the granular slope and bedrock. According to Carson (1977), the angles of the ridges (dislocations along the failure surface between horsts and grabens) should be $45° + \phi/2$ to the translational failure surface. In this simulation, the friction angle of the granular material is assumed to be 10°, leading to the angle of the ridges to equal 50°, as displayed in Figure 6d. The numerical results demonstrate that HMM can well reproduce the spread failure pattern of a natural slope.

4. Microscopic Failure Mechanism

As shown previously, for different inclination angles slopes may exhibit different kinds of failure pattern. At a small inclination angle, the slope may fail as an earth flow, which is the typical failure mode of cohesionless granular materials such as sand or glass beads. With a larger inclination angle, a shear band develops in the slope and propagates backward, which is typical of cohesive materials such as clay. Hence, it can be concluded that, for the same material properties, the slope can show a variety of failure patterns depending on the slope angle.

Therefore, in order to further highlight the influence of material properties on the slope failure mode, several more analyses have been carried out where extreme conditions are considered. Specifically, cohesionless ($k_a = 0$) and highly cohesive ($k_a = 1,2000\,\mathrm{KJ/m^3}$) samples are simulated for various inclination angles as illustrated in

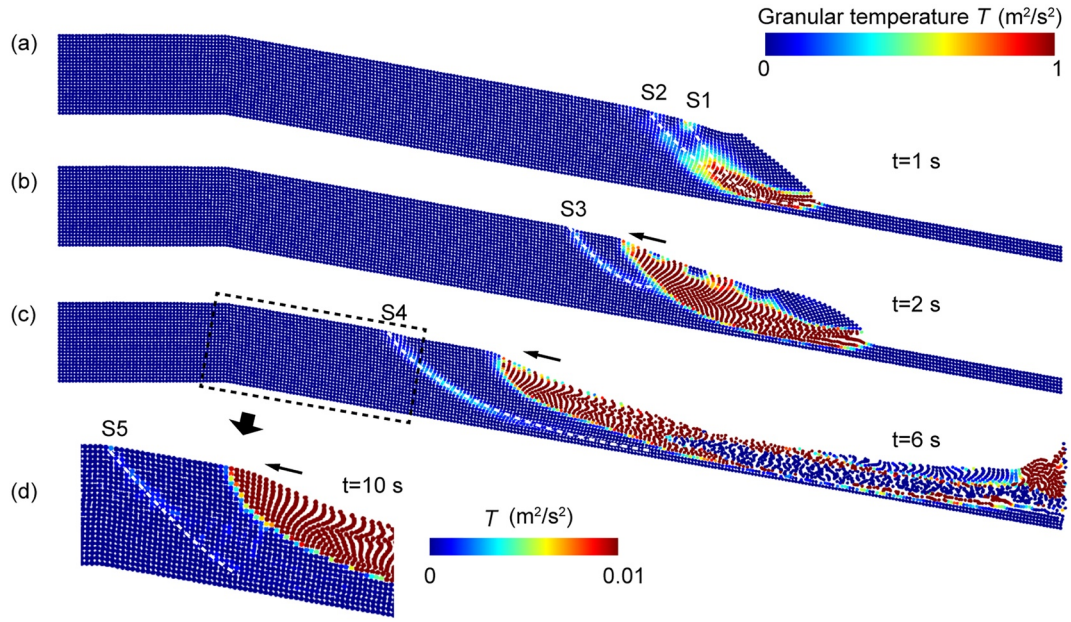

Figure 5. Flowslide failure at a slope inclination of 10°. Contour plot of slope granular temperature at (a) $t = 1$ s; (b) $t = 2$ s; (c) $t = 6$ s. (d) The inset of (c) at $t = 10$s. Labels S1–S5 represent the shear band number.

Figure 7. The highly cohesive sample is presented in Figures 7a, 7c, and 7e for inclination angles of 6°, 12°, and 15°, respectively. When the inclination angle is only 6°, the slope remains stable after removing the confining stress. When the inclination angle increases, the slope fails in a flowslide pattern. The failure of a cohesionless slope is shown in Figures 7b, 7d, and 7f. It can be seen that all these slopes fail in an earth flow pattern. However, when the inclination angle reaches 15°, a translational shear band is formed at the base of the soil layer, which is similar to the one observed in Figure 6. To conclude, under different material properties or slope angles, the slope failure modes are inter changeable, revealing various possible failure modes, that is, earth flows in cohesionless materials and flowslides in cohesive slopes, reflecting the complex nature of the underlying mechanisms. To understand the effect of the influencing factors and reveal the underlying failure mechanisms of different failure patterns, a microscopic analysis is presented in this section.

4.1. Shear Failure

First, we study the earth flow failure pattern. In this pattern, all the elements of the slope undergo two distinct stress states, that is, stable and failure states. Under a stable state, particles are confined and settled under gravity, whereas under a failure state the avalanche propagates through the assembly of particles, showing a high granular temperature which indicates plastic deformation of the materials. Therefore, we compare the difference in behavior of a typical RVE before and after failure, as shown in Figure 8.

The RVE (A1) is selected from the granular slope shown in Figure 4. Figures 8a and 8d show the x-direction displacement of the particles in the RVE. It should be noted that the translation of elements is recorded by the material point whereas the displacement of particles in the RVE is solely caused by the deformation of the material. It can be seen that particles show little movement in the stable state, whereas a large stretching and shearing of the assembly occurs due to failure. Particles in the upper left corner move rightwards, while at the lower right corner they move toward the left. The shape of the element becomes a parallelogram with a shear direction of 150°. The corresponding polar histograms of repulsive (normal contact force $F_n > 0$) and attractive ($F_n < 0$) contact normal distributions of the RVE are plotted in Figures 8b and 8c before failure and Figures 8e and 8f after failure. A repulsive contact indicates that two particles are compressed in the normal direction. For an attractive contact, the contacting particles are stretched and under tensile load. By using polar histograms of the contact normals, the principle orientations of the repulsive and attractive contact forces are determined, indicating the compression and tension orientations of the macroscopic elements. As shown in Figure 8b, the repulsive contact force is mostly distributed vertically, indicating a major orientation of 82.5°, which is nearly perpendicular to

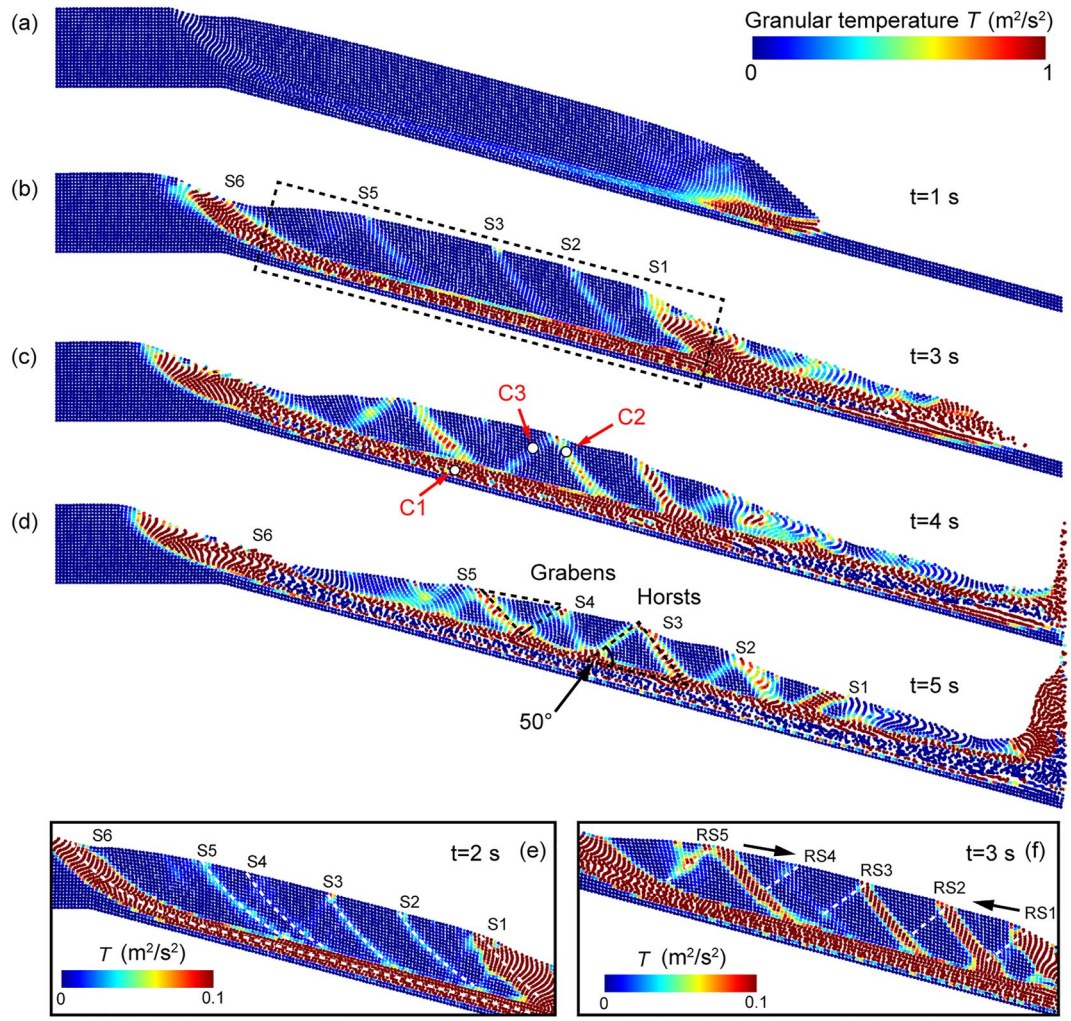

Figure 6. Simulation results for a spread failure. Labels S1–S6 are the indexes of shear bands, while RS1–RS5 are the indexes of reverse shear bands which are nearly perpendicular to shear bands S1–S6. Labels C1–C3 indicate the locations of three typical representative volume elements.

the slope face (6° to the horizontal direction), while the attractive contact forces form around the horizontal direction. The compression is consistent with the gravitational load acting on the slope in the initial stable state and the shear load along the surface, which slightly stretches the soil. When the element fails under shearing, the anisotropy of the repulsive contact normal changes to a principal orientation of 112.5° and the distribution takes on a peanut shape which is roughly at 45° to the shear direction (150°), indicating resistance to shear failure. The attractive contact force distribution shows a principle orientation of around 37.5°, but the number of attractive contacts is much less than the number of repulsive contacts. In conclusion, the RVE shows a typical structure resistant to shear load while the tension load only provokes a slight response. This result indicates that shear failure is the typical RVE failure mode in this slope.

4.2. Tensile Failure

We next consider the failure pattern of the flowslide, which occurs with the increase of the slope inclination. In contrast to the earth flow pattern, the particles tend to show strongly localized deformations for this slope failure mode. To understand the formation and development of the localization, we select three RVEs from a shear band propagated in the flowslide failing slope at the top (B1), medium (B2), and bottom (B3) parts of the band, as shown in Figure 7c. Figures 9a, 9d, and 9g show the x-direction displacements of the particles from the selected RVEs during the development of the shear band. It is found that the particles in the RVEs always show large stretching deformations in the x-direction. Meanwhile, it can be seen that a large crack occurs in B1 (see

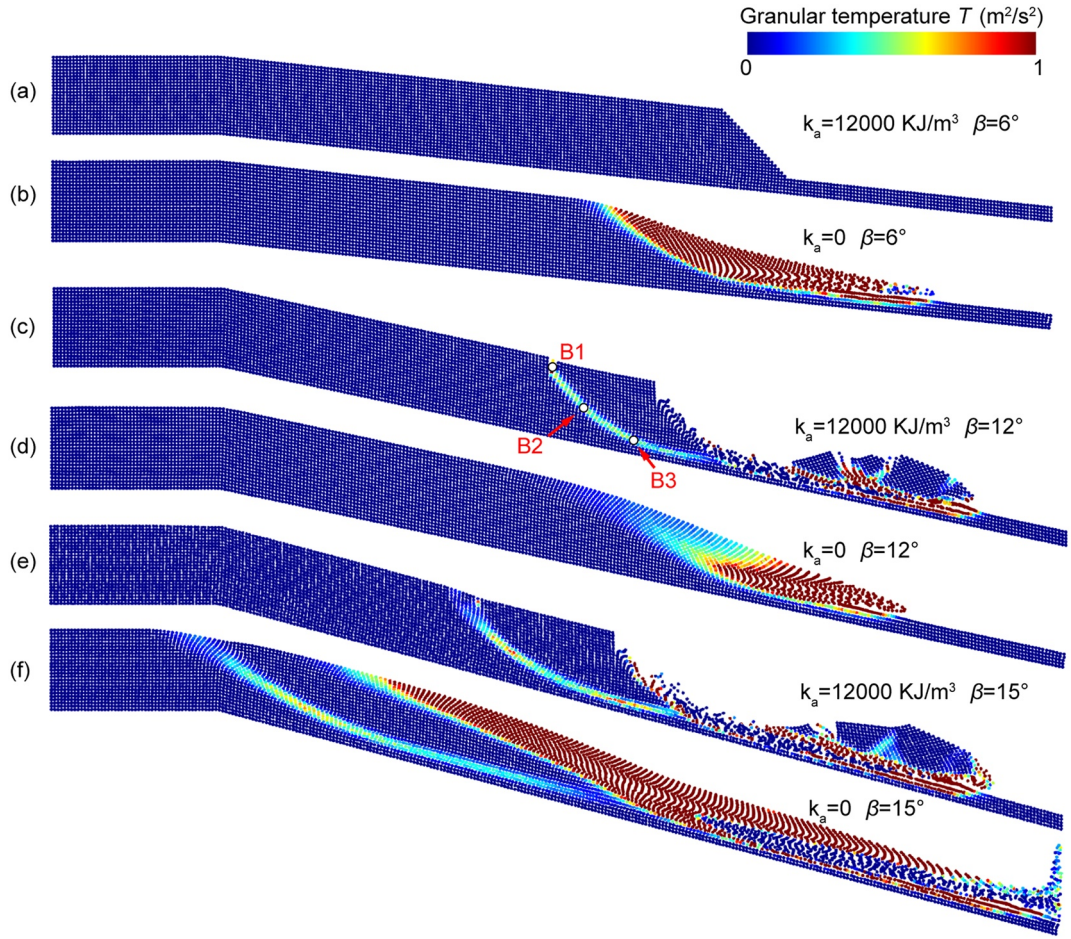

Figure 7. Failure of inclined slopes with different material properties. Labels B1–B3 indicate the locations of three typical representative volume elements.

Figure 9a) and many gaps appear in B2 (as shown in Figure 9d) due to the tensions on the particle assembly. These phenomena are consistent with the observation of tension cracks near the crest of cohesive slopes (He et al., 2019; Quinn et al., 2012; Utili, 2013), indicating the tensile failure of elements.

In comparison with the shear failure pattern shown above, the repulsive and attractive contact normal distributions are displayed in Figure 9. The orientations of the repulsive contact normal distributions are slightly rotated toward 100°, which is nearly vertical to the granular slope surface. It means that the repulsive contacts only weakly resist the shear deformation. As for the attractive contacts, the principal orientation is nearly horizontal as shown in Figures 9f and 9i. However, Figure 9c shows a nearly uniform distribution of the attractive contacts. This uniform distribution is probably caused by the cracking which releases all the tensile stress in the *x*-direction, thereby reducing the development of horizontal attractive contacts. Moreover, it is worth noting that the number of attractive contacts, for instance, as shown in Figures 9c and 9f, is equivalent to or larger than the number of repulsive contacts, indicating a strong cohesion effect in the force chain of the granular assembly.

Obviously, these elements are under strong tensions that are different from the RVEs under shearing. The cracking and large voids developed in Figures 9d and 9g indicate that the microscopic failure mechanism involves cracking and tensile failures. This phenomenon is consistent with observations of the failure of sensitive clays, where tension cracks develop near the surface of the slope, leading to shear bands in flowslide or spread failures (Locat et al., 2011).

4.3. Compound Failure

To provide further clues to the microscopic failure mechanism, we select three RVEs from the spread slope failure shown in Figure 6. RVEs C1-3 are located in the translational shear band (C1), an uphill-propagating shear band

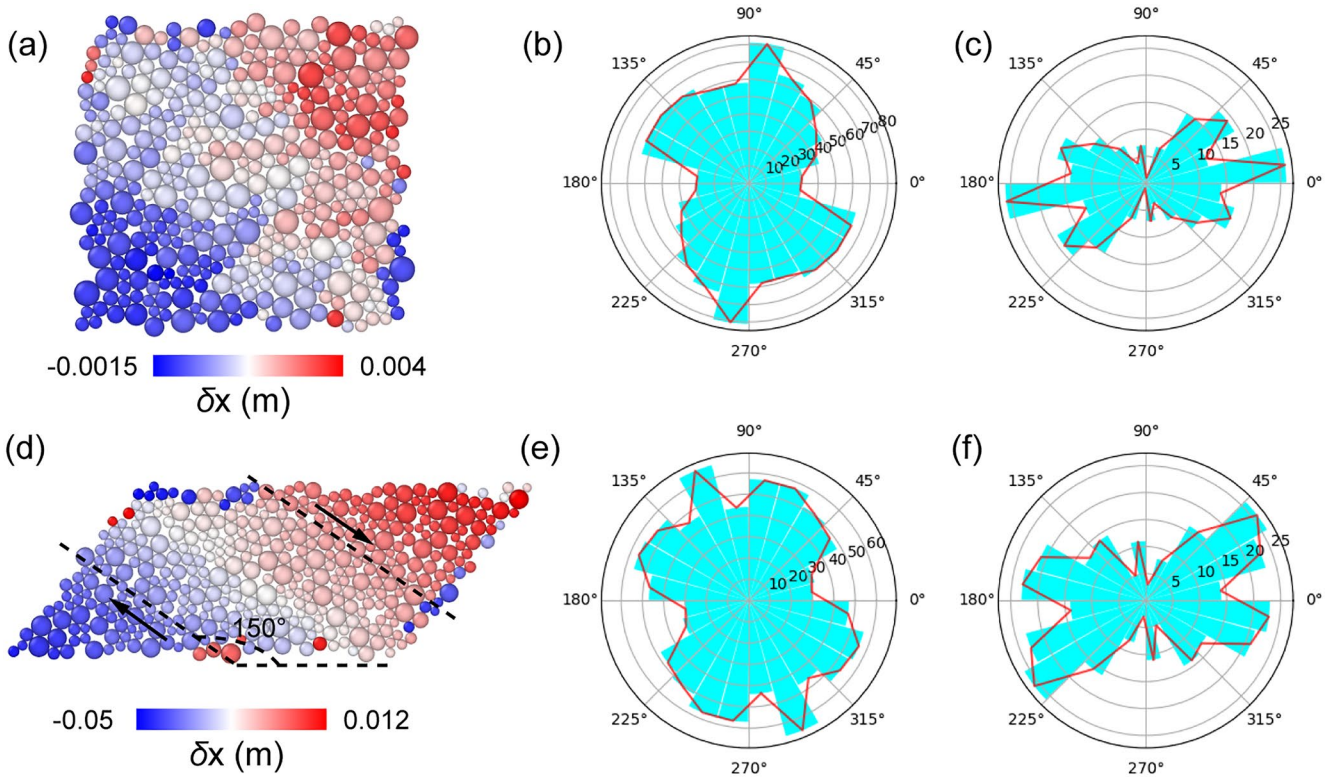

Figure 8. A typical representative volume element in the earth flow failure pattern. (a) *x*-direction displacements after confinement under gravity. (b) Repulsive contact normal distribution of (a). (c) Attractive contact normal distribution of (a). (d) *x*-direction displacements after failure. (e) Repulsive contact normal distribution of (d). (f) Attractive contact normal distribution of (d). The numbers on each circle of the rose diagrams indicate the number of contacts.

(C2), and a reverse shear band (C3), respectively. Figure 10 gives the deformation and contact normal distributions of these RVEs. It is apparent that C1 shows a similar deformation pattern, with respect to the principal orientation of repulsive and attractive contacts, to the shear failure RVE shown in Figures 8a–8c. C2 fails under tension, showing more attractive contacts than repulsive contacts with a principal orientation of 30°. As for C3, a combination of shear and stretching is observed. Many small gaps can be found in Figure 10g, indicating a tension failure pattern, while the contact normal distributions show more repulsive contacts with a similar orientation to Figures 8e and 8f.

Therefore, it is found the initial translational shear band (S6) in the spread slope failure shows a typical shear failure resulting from a frictional shear failure due to the high slope inclination. In contrast, the small shear bands S1–S5 show a similar failure mechanism to uphill-propagating shear bands. The failure of the reverse shear band (RS1-5) shows a relatively complex failure mechanism, where RVEs are stretched due to the loss of support from the crest and toe of the slope and sheared under gravity.

5. Interplay Between Friction and Cohesion

From the observations and analyses above, an inseparable correlation is found between the retrogressive failure pattern and the granular contact state. It is found that an earth flow is highly related to the shear failure of granular materials, which is the typical failure mode of cohesionless granular materials. In such a material, the strength of the assembly is determined by the frictional properties between particles. Meanwhile, with an increase in the inclination angle of a granular slope, shear bands can develop accompanied by stretching of the particle assembly, revealing a tensile failure pattern which is a typical failure feature of cohesive soils such as clay. The strength of these materials is due to the cohesive effect between particles, where the friction can be neglected. These different failure mechanisms indicate an interplay between friction and cohesion effects in a granular system, which results in various macroscopic failure patterns. Therefore, this section explores interplay between the friction and cohesion effects.

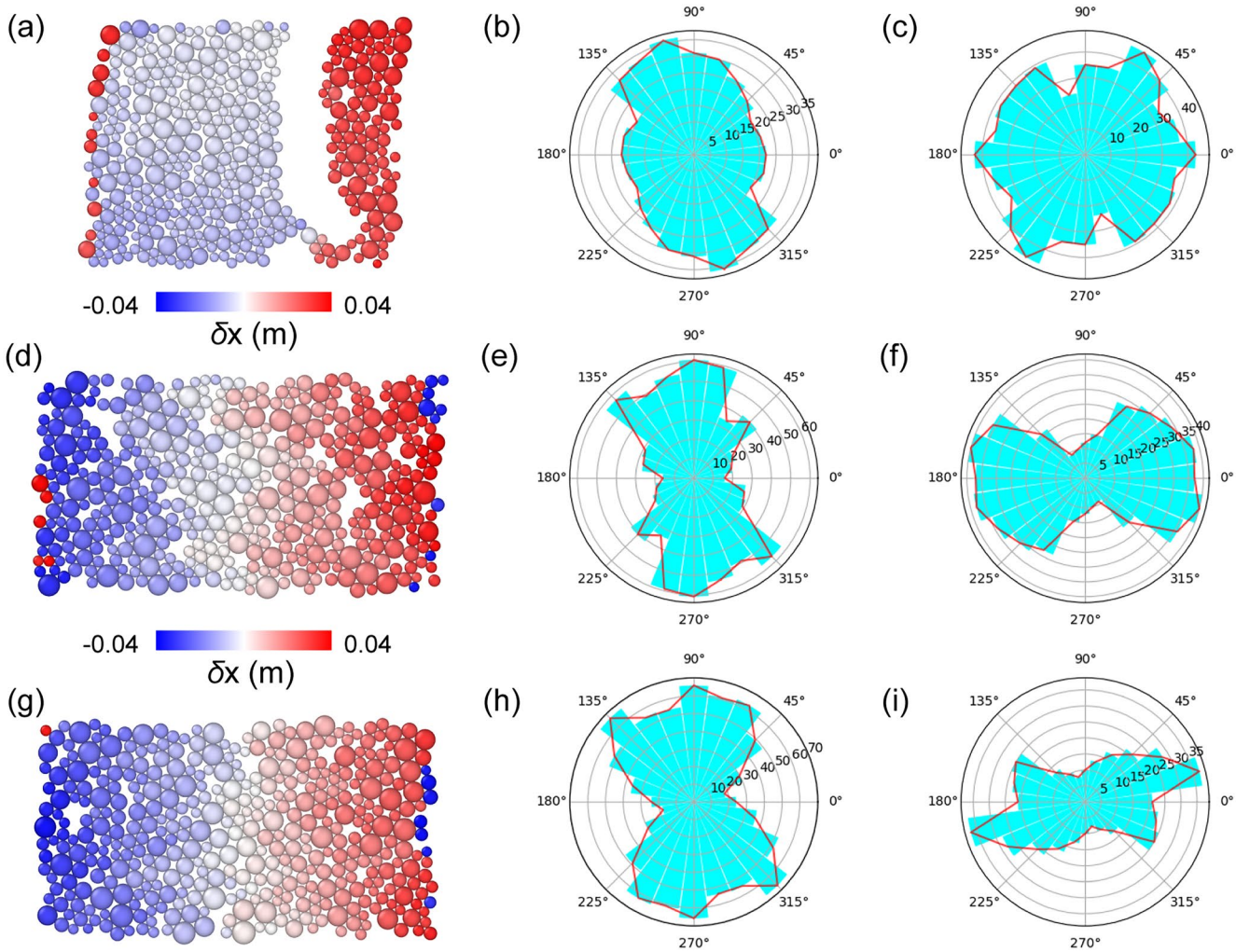

Figure 9. Representative volume elements (RVEs) in a shear band of the cohesive soil slope. (a, d, g) *x*-direction displacements of RVEs at the top (B1), middle (B2), and bottom (B3) of the shear band. Corresponding repulsive contact normal distributions are shown in (b, e, h) and attractive contact normal distributions are shown in (c, f, i). The numbers on each circle of the rose diagrams indicate the number of contacts.

5.1. Statistics of Contact Force Distributions

To explore the interplay between friction and cohesion effects, in this section we examine the normal contact force distributions of RVEs under different failure patterns to distinguish the relative influences of cohesion and friction. Figure 11a shows the normal contact force distributions of three RVEs from the earth flow slope failure (RVE 2838 is the typical RVE presented in Figure 8). It can be seen that the repulsive contact force (F_r) occupies a relatively large proportion of the area under the distribution and that the magnitudes of the repulsive contact forces are in general larger than those of the attractive contact forces (F_c). According to the above analysis of RVE contact normal distributions, these repulsive contact forces mainly contribute to the resistance to shearing during the failure process.

Figure 11b presents the normal contact force distributions of the three RVEs presented in Figure 9, which are taken from a single shear band. These elements undergo large stretch deformations and fail due to tension and cracking. It is seen that the normal contact forces in RVEs 3673 and 3742 show nearly symmetrical distributions, where the proportion of attractive contact forces is much larger than for the sheared elements shown in Figure 11a. With increasing depth, the number of repulsive contact forces increases (as indicated by the direction of the arrow in Figure 11b), resulting in the decreased cracking and tension observed in Figure 9. Therefore, it can be inferred that the ratio of F_c and F_r can be an indicator of the relative cohesion and friction effects in the granular system. When the F_c account for more than half of the contact forces, the granular assembly would be

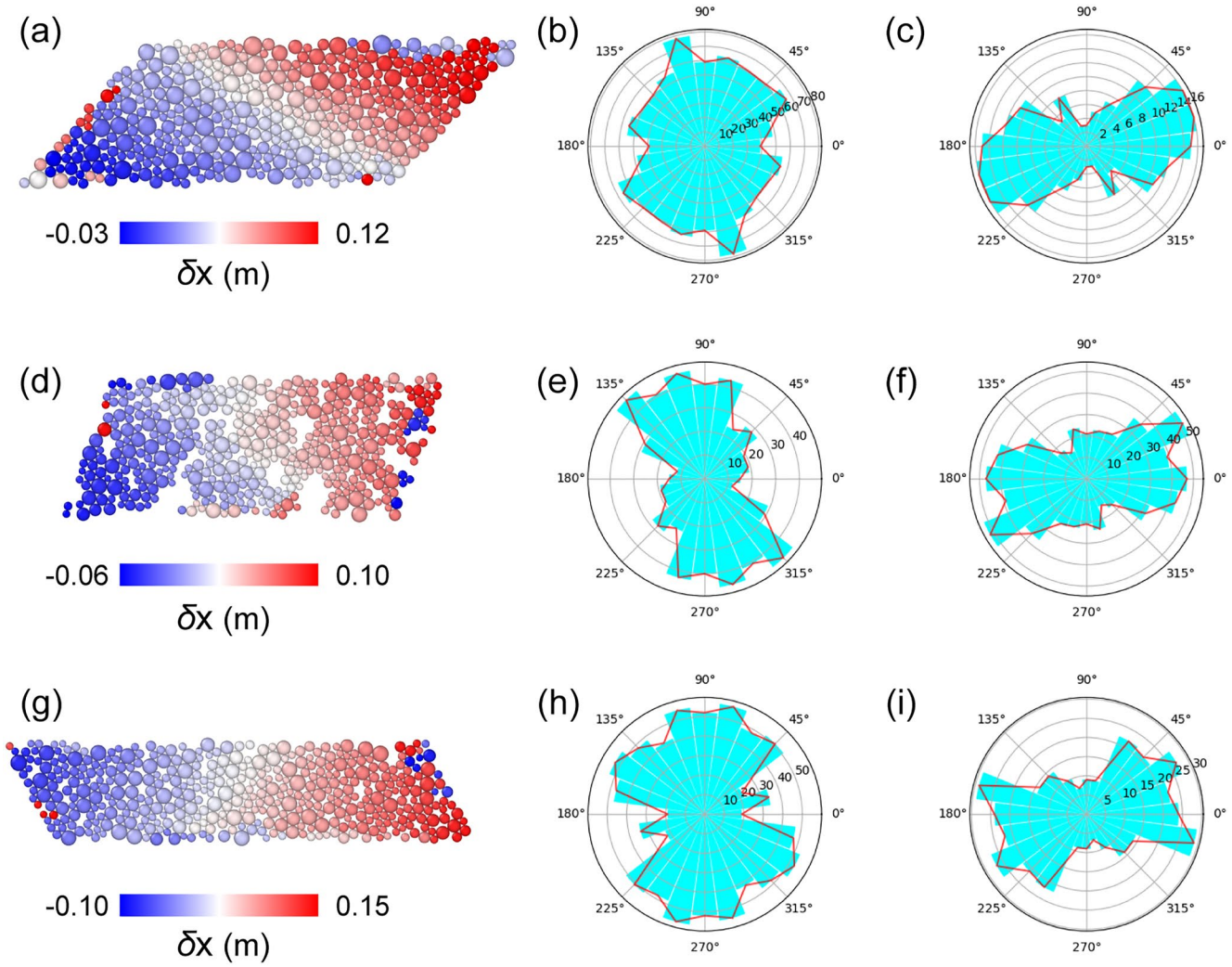

Figure 10. Representative volume elements (RVEs) in a slope experiencing spread failure. (a, d, g) *x*-direction displacements of RVEs from the initial translational shear band (C1), uphill-propagating shear band (C2), and reverse shear band (C3). Corresponding repulsive contact normal distributions are shown in (b, e, h) and attractive contact normal distributions are shown in (c, f, i). The numbers on each circle of the rose diagrams indicate the number of contacts.

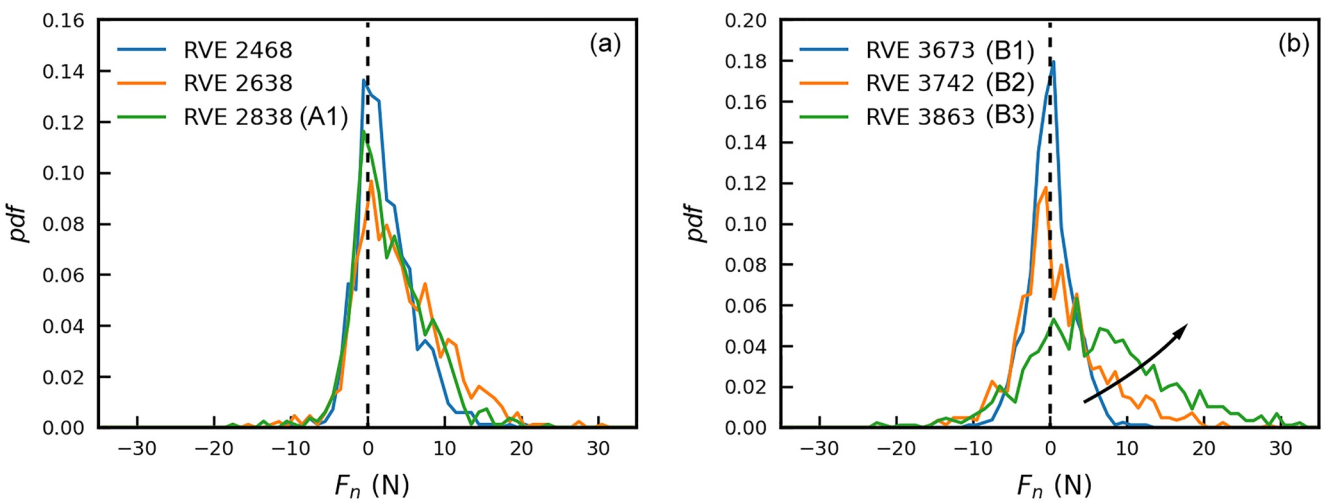

Figure 11. Normal contact force distributions of representative volume elements (RVEs) in (a) an earth flow failure, and (b) a shear band in a flowslide failure.

resistant to stretch and the strength of the element is dominated by the cohesion effect of the granular material. Conversely, when the contact forces are mostly repulsive and the value of the contact force is relatively large, the element would resist shearing. The friction effect is thereby the primary factor that influences the strength of the element. Therefore, the relative percentage of repulsive and attractive normal contact forces is related to the failure mode of the material.

5.2. Indicator for Friction and Cohesion Effect

A novel parameter η is proposed, on the basis of the contact force distributions, to quantify the interplay between friction and cohesion:

$$\eta = \frac{P(F_c)S}{P(F_t)U} \tag{23}$$

where $P(F_c)$ and $P(F_t)$ are the proportions of attractive and repulsive contact forces, respectively, and S and U represent the effects of tension and friction, that is,

$$S = \langle F_c / F_0 \rangle \tag{24}$$

$$U = \langle F_t / \mu F_r \rangle \tag{25}$$

where F_c, F_t, and F_r are the attractive, tangential, and repulsive contact forces acting on each particle, F_0 is the tensile strength of a contact, and $\langle \cdot \rangle$ means the average value of the contacts in RVE. S is called the tension ratio and U is defined in the same way as frictional mobilization which has been widely used in the discussion of shear failure in granular media (Azéma & Radjaï, 2012; Ma et al., 2019; W. Wu et al., 2019). The tangential contact force F_t is introduced in place of the repulsive contact force F_r discussed above, due to the fact that F_t can directly determine the sliding of particles and reflect the friction effect of a granular material. By incorporating F_t, the friction state of the granular assembly can be directly measured and the influence of different inter-particle friction coefficients can be considered. Meanwhile, as each F_r generates one F_t, the proportion of repulsive contact forces $P(F_r)$ is the same as $P(F_t)$. Therefore, $P(F_t)$ can be used in counting the proportion of repulsive normal contacts and in determining η.

Parameters S and U are defined to determine the failure degree of each contact, by normalizing F_c and F_t with the microscopic strength F_0 and μF_r, respectively. F_0 represents the minimum pull-off force necessary for the detachment of two contacting particles. A tensile contact failure therefore occurs when $F_c > F_0$. μF_r refers to the maximum tangential contact force limited by the Coulomb friction law, and particles will slide when $F_t > \mu F_r$.

In summary, η can compare the influence of the contact force distribution and the stability of each contact between F_c and F_t to measure the effect of cohesion and friction quantitatively. A large η indicates a strong cohesion effect where the system may fail during loading via a tensile failure path. Conversely, when η is small, the friction effect is the key factor that dominates the failure of the material.

5.3. Relationship Between η and Macroscopic Failure Pattern

We next apply η to study the interplay between friction and cohesion in the slope failures with different slope inclination angles. η is calculated for each RVE and averaged over the elements with the same depth below the ground surface. This is done at the time when the toe fails (at around 0.6 s after the start of the simulation). Figure 12a plots the distribution of η of RVEs with respect to the normalized slope depth (H/H_0, where H refers to the depth of the element and H_0 is the thickness of the soil layer). A large cohesion effect is seen at the ground surface of the slope and this quickly decreases with increasing depth. This decrease is consistent with our observations of the RVEs experiencing tensile failure, where, with increasing depth, the tendency for cracking and tensile failure decreases.

Figure 12a also shows that, when the slope inclination angle increases, the distribution of η with depth rotates clockwise, resulting in a higher cohesion at the surface and stronger friction at the bottom of the layer. For the surface elements ($H/H_0 < 0.2$), η increases with β, and the failure pattern changes from an earth flow to a flowslide. For the bottom elements, η decreases with increasing inclination angle, indicating an increased tendency for shear failure. When the inclination angle reaches 15°, a spread failure occurs, where the bottom

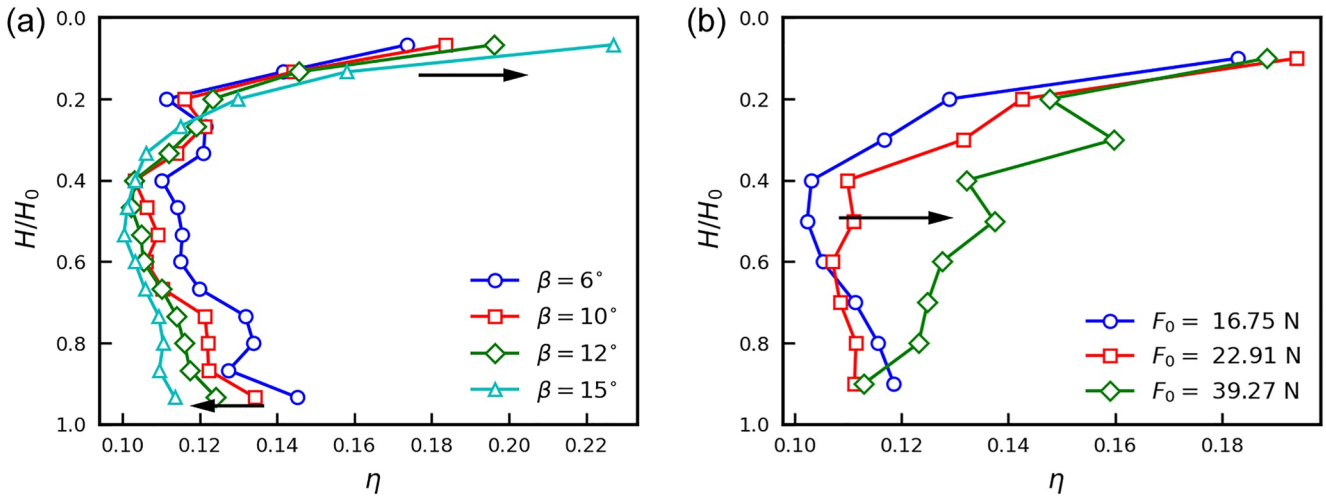

Figure 12. Distribution of η with depth below the ground surface. (a) As a function of inclination angle; (b) as a function of tensile strength.

RVEs ($H/H_0 > 0.8$) fail under shearing, forming the initial large translational shear band as shown in Figure 6. Therefore, it can be concluded that η performs well as an indicator in describing the cohesion and friction effect of granular materials in a microscopic view. The observation on η also reveals that the transition between cohesion and friction near the surface is highly related to the change in macroscopic failure pattern, e.g., the transition from earth flow to flowslide, and the formation of the bottom shear band as seen in the spread failure. We also examine the application of η with varying material properties. Figure 12b shows profiles of η for different tensile strengths F_0 (resulting from different values of cohesion energy density k_a). It can be seen that η shifts to the right with increasing tensile strength (larger value of F_0) for RVEs at all depths, proving that η may also capture the influence between different material properties.

Figure 13 further explains the distribution of η by showing the distribution of $P(F_c)$, $P(F_t)$, S and U versus the mean stress of RVEs. The mean stress characterizes the confining pressure experienced by the element, which increases with depth of the soil. As shown in Figures 13a and 13b, a significant reduction of $P(F_c)$ and growth of $P(F_t)$ is found with an increase in mean stress. When the mean stress reaches 100 kPa, $P(F_c)$ and $P(F_t)$ gradually become stable. The correlation between mean stress and $P(F_c)$, and $P(F_t)$, originates from the packing of the granular assembly. When the mean stress is small, the packing of the assembly is relatively loose and the contacts between particles are mostly maintained by the attractive forces. When the mean stress increases, the packing gets denser and the attractive forces between particles are converted into repulsive and tangential forces. In Figure 13c, S shows a linear increase with the mean stress, meaning more cohesive contacts are approaching failure. As for the distribution of U, no correlation is found with the mean stress of the RVEs. Therefore, with an increase of the mean stress, $P(F_c)$ decreases and $P(F_t)$ increases, producing a higher η at the surface and a smaller η at the bottom of the soil layer. S increases with a higher mean stress, which may produce a larger η. However, due to the extremely strong influence of $P(F_c)$ and $P(F_t)$ at the ground surface, and a stable state after the mean stress reaches around 100 kPa, S only causes a slight increase in η at the bottom of the soil layer. Since U does not change with mean stress, it contributes little to the value of η at different depths.

Figure 13 also demonstrates the influence of the slope inclination angle β on the distribution of $P(F_c)$, $P(F_t)$, S, and U. It can be seen that β has little influence on the distribution of $P(F_c)$, $P(F_t)$, and S, but results in an increase in U for larger values of β. This increase results in a decrease of η according to Equation 23 and the leftward shift of the bottom of the curves shown in Figure 12a, which is related to the formation of the basal failure surface. However, for the ground surface, η shows a tendency to increase regardless of the influence of U. This is because the mean stress is relatively small and the changes in $P(F_c)$ and $P(F_t)$ are quite significant. When the inclination angle β increases, the mean stress decreases, leading to an increase in $P(F_c)$ and a reduction in $P(F_t)$. As a result, the surface elements show an increase of η, which is related to the development of shear bands in the flowslide and spread failure patterns.

When the material properties change, the distributions of $P(F_c)$, $P(F_t)$, S, and U will be different. As shown in Figure 14, when F_0 increases, that is, there is a larger cohesive strength, $P(F_c)$ increases and $P(F_t)$ decreases.

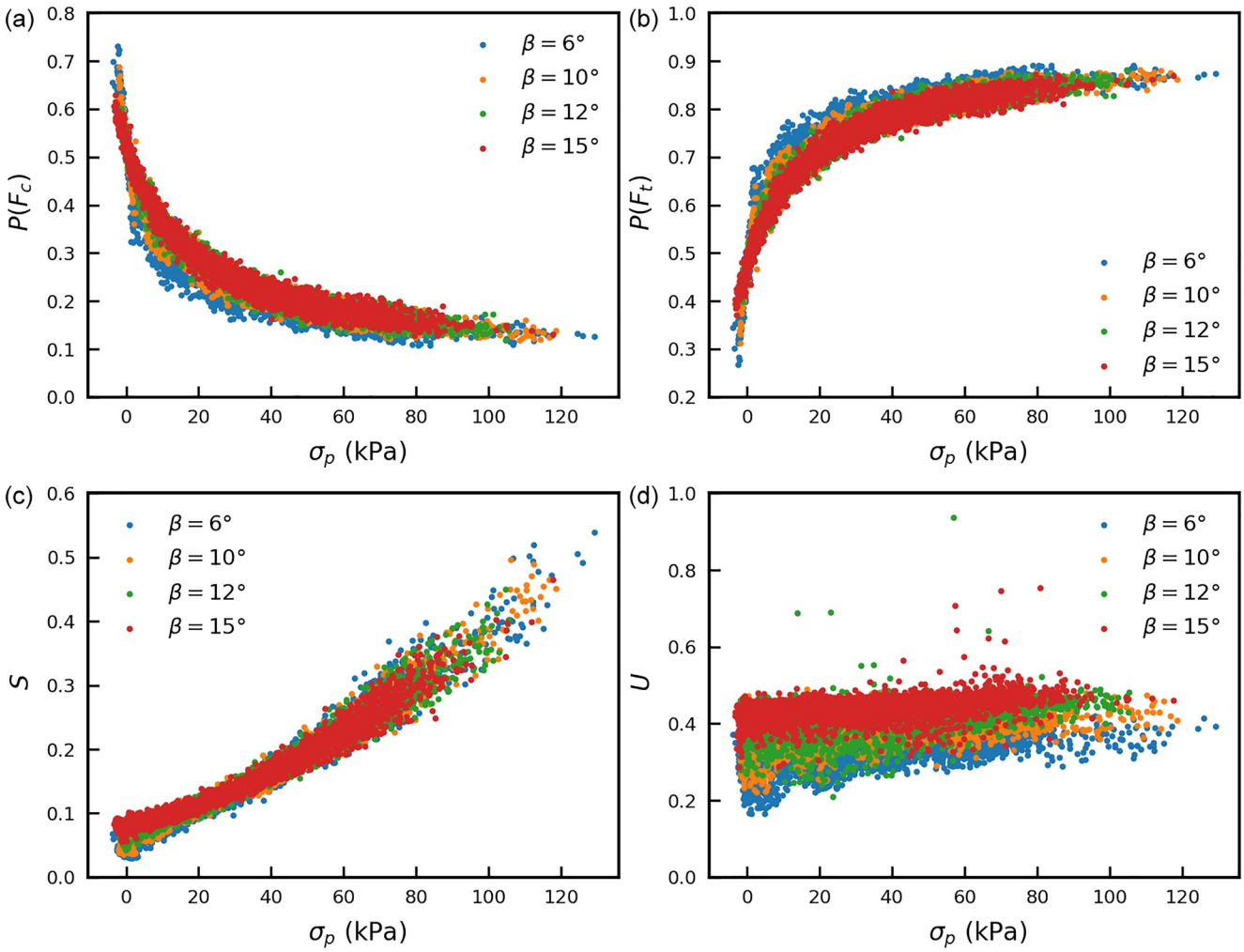

Figure 13. Distributions of $P(F_c)$, $P(F_t)$, S, and U versus mean stress of the representative volume element for different slope inclination angles.

Due to the higher cohesive strength between contacts, S shows a decrease with respect to F_0 for different mean stresses. Meanwhile, U also decreases with an increasing cohesive strength (larger F_0), since part of the shear load is taken by attractive contacts when the cohesive strength increases. The changes in $P(F_c)$, $P(F_t)$, and U with larger cohesive strengths all contribute to an increase of η, leading to a right-hand shift in η, as shown in Figure 12. However, due to the decrease of S, the increase of η at the bottom part of the soil is limited.

Through the analysis of $P(F_c)$, $P(F_t)$, S, and U versus the mean stress of RVEs under different inclination angles and cohesive strengths, it is concluded that the surface elements of the slope are strongly correlated to the variation of $P(F_c)$, $P(F_t)$ and confinement, whereas the bottom elements are relatively more affected by S and U.

5.4. Spectrum of Retrogressive Slope Failure

We apply η in interpreting the pattern transition in retrogressive slope failure. According to the analysis from the last section, the value of η for the surface elements of the slope is related to the transition between earth flow and flowslide. In contrast, the value of η near the bottom of the soil layer is related to the occurrence of spread failure. Therefore, we defined η_t and η_b to represent the average value of η for the top and bottom 20% of elements in each slope. Figure 15 shows all the simulations carried out in this study with respect to η_t and η_b. For each point, the x-axis indicates the slope inclination angle, and the y-axis indicates F_0 (i.e., the tensile strength of contacts). The symbol used to represent each point indicates the slope failure pattern, while the color of the symbol indicates the value of η. The stable case is marked as a black star and the value of η is not discussed in this study.

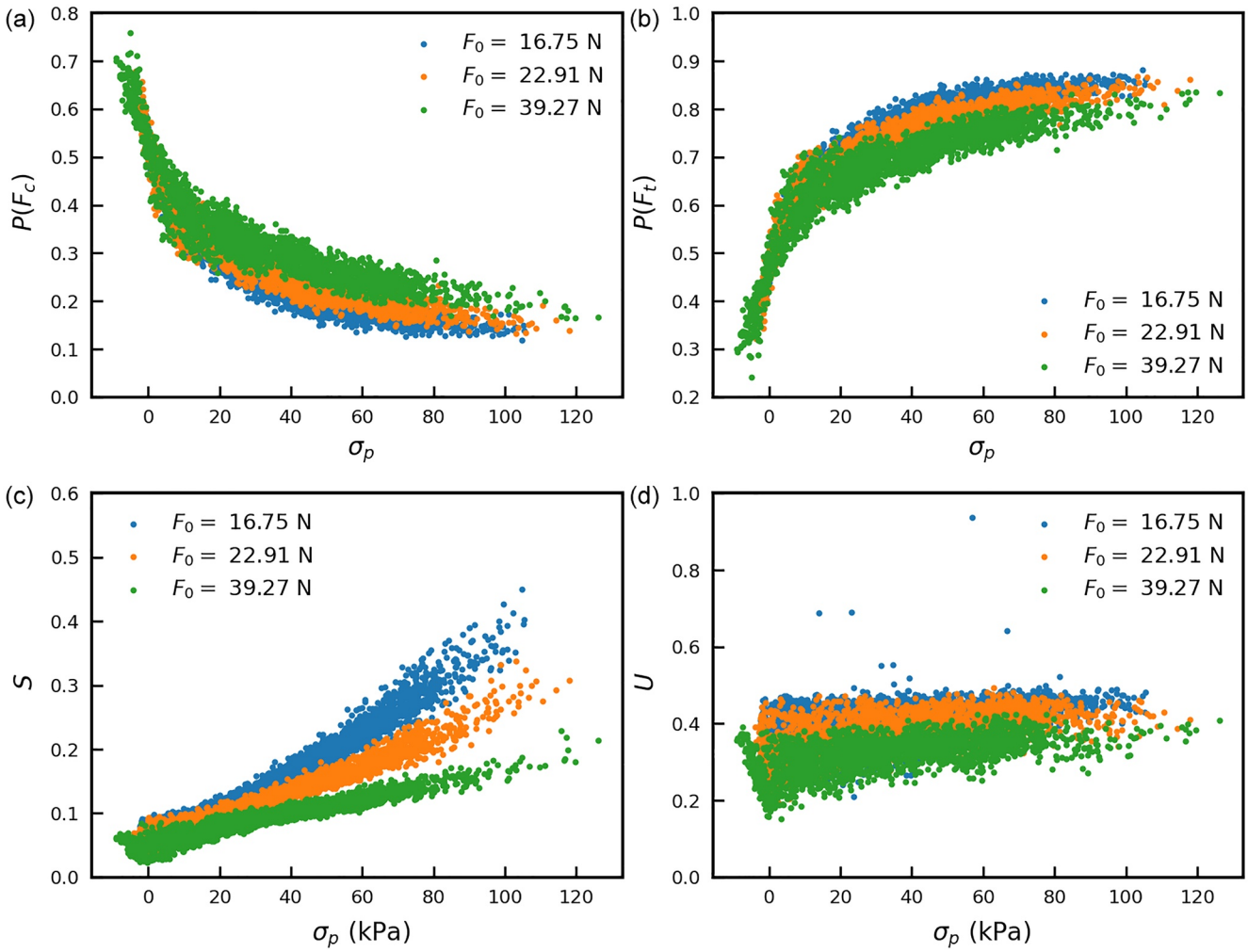

Figure 14. Distributions of $P(F_c)$, $P(F_t)$, S, and U versus the mean stress of representative volume element for different value of F_0.

As seen in Figure 15a, slopes with a lower β and a smaller F_0 show a smaller η_t, indicating a strong friction effect. These slopes finally fail in an earth flow pattern. In contrast, for slopes with a higher β and larger F_0, the failure pattern changes from earth flow to a localization failure pattern, which includes both flowslide and spread failure patterns. The transition between earth flow and shear banding occurs at around $\eta_t \approx 0.15$ in this study. Figure 15b presents the distribution of η_b, showing a smaller value at a high β and a low F_0. When these slopes fail, a large basal failure surface forms, producing a spread failure pattern in the macroscopic view. The transition between spread and earth flow or flowslide is seen at around $\eta_b \approx 0.11$. However, there are two points with low η_b that do not fall within the spread failure area, as shown in Figure 15b. This is because an F_0 is zero in these slopes, leading to zero $P(F_c)$ and the influence of strength parameter S and U being hidden.

Based on the indicator η and the simulation results, we finally summarize a spectrum of retrogressive failure patterns, as shown in Figure 16. Different retrogressive failure patterns can be categorized by three curves, L1–L3. L1 represents the stability of the slope. Slopes with a shallow inclination angle or high cohesion tend to be stable. Meanwhile, L2 and L3 are related to the friction and cohesion effects in the bottom and surface elements. L2 indicates the development of the bottom failure surface. In this study, the bottom failure surface is always controlled by the frictional effect, showing shear failure in a microscopic view and a small η_b. L3 is the boundary between earth flow and shear band retrogressive failure patterns. The formation of this curve is determined by the surface failure pattern. When the slope inclination angle is high and the material is more cohesive, a shear band develops, leading to a flowslide failure. Conversely, earth flows tend to occur for low slope inclination angles with a lower cohesive strength, showing flow failure at the surface elements. Finally, with these curves, the

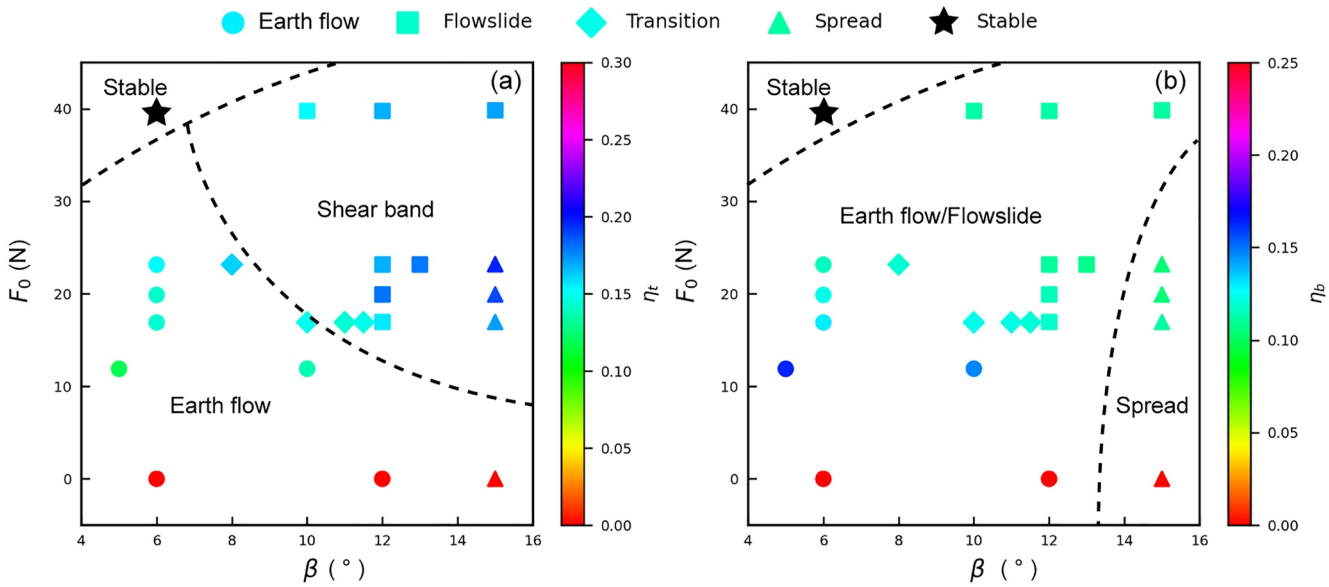

Figure 15. Distribution of η in slopes as a function of slope inclination angle and material properties. (a) The distribution of η_t; (b) the distribution of η_b.

spectrum of retrogressive failure patterns is divided into five major parts, including stable, earth flow, flowslide, spread and the right bottom part, which indicates a combination of earth flow and spread failure.

The spectrum proposed in this study unifies the different retrogressive failure patterns based on multiscale modeling. Different failure patterns are distinguished by analyzing the interplay between friction and cohesion between particles. It is found that the friction and cohesion effect does not purely rely on the material parameters of the particles, but can also be significantly influenced by the stress state in the slope. Hence, the slope may show different dominant effects at the surface and bottom of the soil layer. The surface failure transitions from earth flow to localization failure when the dominant effect changes from friction to cohesion. In contrast, the bottom of the slope is mainly dominated by the frictional effect and develops a large bottom failure surface when failing.

This investigation helps in understanding the variety of failure patterns in natural slopes. The surface soil property controls the development of the shear band. For a dry granular material, no shear band develops and the slope always fails in an earth flow manner. When the soil is purely cohesive, for instance, sensitive clay, the frictional effect is weak and tensile failure is prone to occur, leading to more flowslide failures. If the material is both frictional and cohesive, the failure pattern can vary from earth flow to flowslide depending on stress state. In contrast to the surface failure pattern, the bottom of the slope always fails under shear. In a sensitive clay slope, the bottom soil can be easily sheared to a failure state, leading to a nearly horizontal translational shear band and the development of a spread failure.

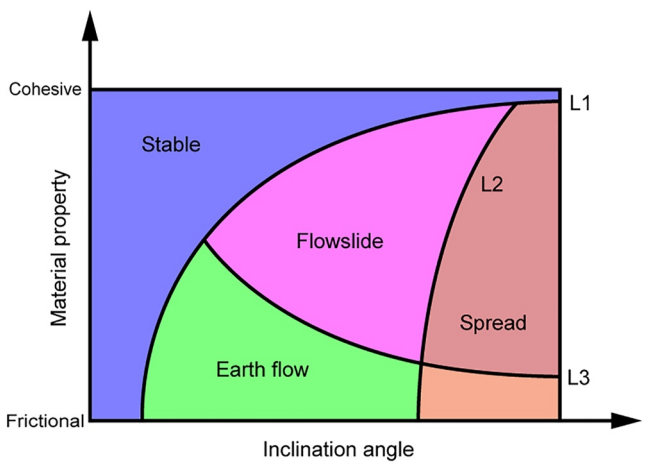

Figure 16. A spectrum of retrogressive slope failure.

6. Conclusions

In this work, we employ multiscale analysis to seek a profound and systematic comprehension of retrogressive slope failure mechanisms. Without relying on a phenomenological constitutive law, the implementation of HMM may appropriately reproduce all kinds of retrogressive failure patterns in granular slopes. With the alteration of slope inclination, three major types of slope failure patterns are reproduced: earth flow, flowslide, and spread failure. A microscopic analysis is adopted to explore the physical mechanism of different failure patterns. It is recognized that shear and tensile failures are two important features in earth flows and flowslide failures. As shear and tensile failures respectively correspond to the friction and cohesion characteristics of granular materials, it is indicated that the cohesion and friction effects are

key to different retrogressive failure patterns. Through the statistics of the normal contact force distribution of RVEs, it is found that microscopic shear or tensile failures are related to the proportion and value of repulsive and attractive contact forces.

In this respect, a novel parameter η is proposed to quantitatively measure the interplay between friction and cohesion. By summarizing the values of η at different depths of the slope, it is found that the transition between flow and shear band is highly related to the cohesion and friction properties of surface elements. In contrast, the development of the bottom failure surface in spread failure is related to the frictional properties of bottom elements. Therefore, by looking into the η values of the top and bottom elements in failure, different retrogressive failure patterns can be distinguished with varying slope inclination angle and/or material properties. The various macroscopic failure patterns can be categorized into earth flow or shear band failure (including flowslide and spread) by the value of η of the surface elements, while the critical line between spread and earth flow or flowslide can be classified by considering the value of η of the bottom elements. Based on this indicator, a spectrum of retrogressive slope failure is established, showing the interplay between friction and cohesion effect in retrogressive slope failure. This study provides a new view on retrogressive slope failure, based on the interplay between friction and cohesion which can be helpful in understanding the complex failure mechanisms in natural landslide hazards.

Data Availability Statement

The data related to this paper can be accessed via an online repository from the link https://doi.org/10.5281/zenodo.7303629, or by contacting the corresponding authors. The software used for this study is open source and publicly available as cited in the main text.

Acknowledgments
The authors wish to acknowledge the National Natural Science Foundation of China (Grants 51979270 and 51709258) and the CAS Pioneer Hundred Talents Program for their financial support.

References

Azéma, E., & Radjaï, F. (2012). Force chains and contact network topology in sheared packings of elongated particles. *Physical Review E—Statistical, Nonlinear, and Soft Matter Physics*, *85*(3), 1–12. https://doi.org/10.1103/PhysRevE.85.031303

Carson, M. A. (1977). On the retrogression of landslides in sensitive muddy sediments. *Canadian Geotechnical Journal*, *14*(4), 582–602.

Carson, M. A. (1979). On the retrogression of landslides in sensitive muddy sediments: Reply. *Canadian Geotechnical Journal*, *16*(2), 431–444. https://doi.org/10.1139/t79-047

Chandel, A., Singh, M., & Thakur, V. (2021). Retrogressive failure of reservoir rim sandy slopes induced by steady-state seepage condition. *Indian Geotechnical Journal*, *51*(4), 705–718. https://doi.org/10.1007/s40098-021-00502-1

Cuomo, S., Ghasemi, P., Martinelli, M., & Calvello, M. (2019). Simulation of liquefaction and retrogressive slope failure in loose coarse-grained material. *International Journal of Geomechanics*, *19*(10), 04019116. https://doi.org/10.1061/(asce)gm.1943-5622.0001500

Daerr, A., & Douady, S. (1999). Two types of avalanche behavior in granular media. *Nature*, *399*(6733), 241–243. https://doi.org/10.1038/20392

Dey, R., Hawlader, B., Phillips, R., & Soga, K. (2015). Large deformation finite-element modeling of progressive failure leading to spread in sensitive clay slopes. *Géotechnique*, *65*(8), 657–668.

Eke, E., Viparelli, E., & Parker, G. (2011). Field-scale numerical modeling of breaching as a mechanism for generating continuous turbidity currents. *Geosphere*, *7*(5), 1063–1076. https://doi.org/10.1130/GES00607.1

Germanovich, L. N., Kim, S., & Puzrin, A. M. (2016). Dynamic growth of slip surfaces in catastrophic landslides. *Proceedings of the Royal Society A: Mathematical, Physical & Engineering Sciences*, *472*(2185), 20150758. https://doi.org/10.1098/rspa.2015.0758

Glimsdal, S., L'Heureux, J. S., Harbitz, C. B., & Løvholt, F. (2016). The 29th January 2014 submarine landslide at Statland, Norway—Landslide dynamics, tsunami generation, and run-up. *Landslides*, *13*(6), 1435–1444. https://doi.org/10.1007/s10346-016-0758-7

Goren, L., & Aharonov, E. (2007). Long runout landslides: The role of frictional heating and hydraulic diffusivity. *Geophysical Research Letters*, *34*(7). https://doi.org/10.1029/2006gl028895

Guo, N., Yang, Z., Yuan, W., & Zhao, J. (2021a). A coupled SPFEM/DEM approach for multiscale modeling of large-deformation geomechanical problems. *International Journal for Numerical and Analytical Methods in Geomechanics*, *45*(5), 648–667. https://doi.org/10.1002/nag.3175

Guo, N., & Zhao, J. (2014). A coupled FEM/DEM approach for hierarchical multiscale modeling of granular media. *International Journal for Numerical Methods in Engineering*, *99*(11), 789–818. https://doi.org/10.1002/nme.4702

Guo, X., Peng, C., Wu, W., & Wang, Y. (2021). Unified constitutive model for granular-fluid mixture in quasi-static and dense flow regimes. *Acta Geotechnica*, *16*(3), 775–787. https://doi.org/10.1007/s11440-020-01044-1

He, Y., Liu, Y., Zhang, Y., & Yuan, R. (2019). Stability assessment of three-dimensional slopes with cracks. *Engineering Geology*, *252*, 136–144.

Hu, Y., Li, T. M., Anderson, L., Ragan-Kelley, J., & Durand, F. (2019). Taichi: A language for high-performance computation on spatially sparse data structures. *ACM Transactions on Graphics*, *38*(6), 1–16.

Kloss, C., Goniva, C., Hager, A., Amberger, S., & Pirker, S. (2012). Models, algorithms, and validation for opensource DEM and CFD-DEM. *Progress in Computational Fluid Dynamics, an International Journal*, *12*(2–3), 140–152.

Liang, W., & Zhao, J. (2019a). Coupled MPM/DEM multiscale modeling geotechnical problems involving large deformation. In *16th Asian Regional Conference on sSoil Mechanics and Geotechnical Engineering*.

Liang, W., & Zhao, J. (2019b). Multiscale modeling of large deformation in geomechanics. *International Journal for Numerical and Analytical Methods in Geomechanics*, *43*(5), 1080–1114. https://doi.org/10.1002/nag.2921

Liu, C., Sun, Q., & Yang, Y. (2017). Multi-scale modeling of granular pile collapse by using material point method and discrete element method. *Procedia Engineering*, *175*, 29–35. https://doi.org/10.1016/j.proeng.2017.01.009

Lo, K. Y. (1972). An approach to the problem of progressive failure. *Canadian Geotechnical Journal*, *9*(4), 407–429.

Locat, A., Leroueil, S., Bernander, S., Demers, D., Jostad, H. P., & Ouehb, L. (2011). Progressive failures in eastern Canadian and Scandinavian sensitive clays. *Canadian Geotechnical Journal*, *48*(11), 1696–1712. https://doi.org/10.1139/t11-059

Løvholt, F., Pedersen, G., Harbitz, C. B., Glimsdal, S., & Kim, J. (2015). On the characteristics of landslide tsunamis. *Philosophical Transactions of the Royal Society A: Mathematical, Physical, & Engineering Sciences*, *373*, 2053. https://doi.org/10.1098/rsta.2014.0376

Ma, G., Chen, Y., Yao, F., Zhou, W., & Wang, Q. (2019). Evolution of particle size and shape towards a steady state: Insights from FDEM simulations of crushable granular materials. *Computers and Geotechnics*, *112*, 147–158. https://doi.org/10.1016/j.compgeo.2019.04.022

Mitchell, R. J., & Markell, A. R. (1974). Flowsliding in sensitive soils. *Canadian Geotechnical Journal*, *11*(1), 11–31. https://doi.org/10.1139/t74-002

Nicot, F., Hadda, N., Guessasma, M., Fortin, J., & Millet, O. (2013). On the definition of the stress tensor in granular media. *International Journal of Solids and Structures*, *50*(14–15), 2508–2517.

Paesold, M., Bassom, A., Regenauer-Lieb, K., & Veveakis, M. (2016). Conditions for the localization of plastic deformation in temperature sensitive viscoplastic materials. *Journal of Mechanics of Materials and Structures*, *11*(2), 113–136.

Puzrin, A. M. (2016). Simple criteria for plowing and runout in post-failure evolution of submarine landslides. *Canadian Geotechnical Journal*, *53*(8), 1305–1314.

Puzrin, A. M., Gray, T. E., & Hill, A. J. (2017). Retrogressive shear band propagation and spreading failure criteria for submarine landslides. *Géotechnique*, *67*(2), 95–105. https://doi.org/10.1680/jgeot.15.P.078

Qi, X., Xu, Q., & Liu, F. (2018). Analysis of retrogressive loess flowslides in Heifangtai, China. *Engineering Geology*, *236*, 119–128. https://doi.org/10.1016/j.enggeo.2017.08.028

Quinn, P. E., Diederichs, M. S., Rowe, R. K., & Hutchinson, D. J. (2012). Development of progressive failure in sensitive clay slopes. *Canadian Geotechnical Journal*, *49*(7), 782–795. https://doi.org/10.1139/T2012-034

Richer, B., Saeidi, A., Boivin, M., & Rouleau, A. (2020). Overview of retrogressive landslide risk analysis in sensitive clay slope. *Geosciences*, *10*(8), 1–16. https://doi.org/10.3390/geosciences10080279

Sima, J., Jiang, M., & Zhou, C. (2014). Numerical simulation of desiccation cracking in a thin clay layer using 3D discrete element modeling. *Computers and Geotechnics*, *56*, 168–180.

Tavenas, F. (1984). Landslides in Canadian sensitive clays—A state-of-the-art. In *Proceedings of the 4th International Symposium on Landslides* (pp. 16–21).

Utili, S. (2013). Investigation by limit analysis on the stability of slopes with cracks. *Géotechnique*, *63*(2), 140–154.

Van Den Berg, J. H., Van Gelder, A., & Mastbergen, D. R. (2002). The importance of breaching as a mechanism of subaqueous slope failure in fine sand. *Sedimentology*, *49*(1), 81–95. https://doi.org/10.1111/j.1525-139X.2006.00168.x-i1

Vardon, P. J., Wang, B., & Hicks, M. A. (2017). Slope failure simulations with MPM. *Journal of Hydrodynamics*, *29*(3), 445–451. https://doi.org/10.1016/S1001-6058(16)60755-2

Vardoulakis, I. (2002). Dynamic thermo-poro-mechanical analysis of catastrophic landslides. *Géotechnique*, *52*(3), 157–171.

Varnes, D. J. (1958). Landslide types and processes. *Landslides and Engineering Practice*, *24*, 20–47.

Wang, B., Vardon, P. J., & Hicks, M. A. (2016). Investigation of retrogressive and progressive slope failure mechanisms using the material point method. *Computers and Geotechnics*, *78*, 88–98. https://doi.org/10.1016/j.compgeo.2016.04.016

Wang, B., Vardon, P. J., & Hicks, M. A. (2018). Rainfall-induced slope collapse with coupled material point method. *Engineering Geology*, *239*, 1–12.

Wang, D., Randolph, M. F., & White, D. J. (2013). A dynamic large deformation finite element method based on mesh regeneration. *Computers and Geotechnics*, *54*, 192–201.

Wang, D., Wang, B., Jiang, Q., Guo, N., Zhang, W., & He, K. (2022). Large deformation slope failure—A perspective from multiscale modeling. *Computers and Geotechnics*, *150*, 104886.

Wu, H., Guo, N., & Zhao, J. (2017). Multiscale modeling and analysis of compaction bands in high-porosity sandstones. *Acta Geotechnica*. https://doi.org/10.1007/s11440-017-0560-2

Wu, H., Papazoglou, A., Viggiani, G., Dano, C., & Zhao, J. (2020). Compaction bands in Tuffeau de Maastricht: Insights from X-ray tomography and multiscale modeling. *Acta Geotechnica*, *15*(1), 39–55. https://doi.org/10.1007/s11440-019-00904-9

Wu, H., Zhao, J., & Guo, N. (2018). Multiscale insights into borehole instabilities in high-porosity sandstones. *Journal of Geophysical Research: Solid Earth*, *123*(5), 3450–3473. https://doi.org/10.1029/2017JB015366

Wu, W., Ma, G., Zhou, W., Wang, D., & Chang, X. (2019). Force transmission and anisotropic characteristics of sheared granular materials with rolling resistance. *Granular Matter*. https://doi.org/10.1007/s10035-019-0938-y

Xu, Y., Nie, L., Dai, S. L., & Zhang, M. (2011). Formation and evolution of Chaancun landslide in Dalian City, China. *Advanced Materials Research*, *250–253*, 1395–1399. https://doi.org/10.4028/www.scientific.net/AMR.250-253.1395

Zhang, W., & Puzrin, A. M. (2021). Depth integrated modeling of submarine landslide evolution. *Landslides*, *18*(9), 3063–3084.

Zhang, W., Wang, D., Randolph, M. F., & Puzrin, A. M. (2016). Dynamic propagation criteria for catastrophic failure in planar landslides. *International Journal for Numerical and Analytical Methods in Geomechanics*, *40*(17), 2312–2338.

Zhang, X., Sloan, S. W., & Oñate, E. (2018). Dynamic modeling of retrogressive landslides with emphasis on the role of clay sensitivity. *International Journal for Numerical and Analytical Methods in Geomechanics*, *42*(15), 1806–1822. https://doi.org/10.1002/nag.2815

Zou, Y., Ma, G., Mei, J., Zhao, J., & Zhou, W. (2022). Microscopic origin of shape-dependent shear strength of granular materials: A granular dynamics perspective. *Acta Geotechnica*, *17*(7), 2697–2710.